

# Built-in and induced polarization across $\text{LaAlO}_3/\text{SrTiO}_3$ heterojunctions

Guneeta Singh-Bhalla,<sup>1,2,3,4,\*</sup> Christopher Bell,<sup>3,5</sup> Jayakanth Ravichandran,<sup>6,2</sup> Wolter Siemons,<sup>1</sup> Yasuyuki Hikita,<sup>3</sup> Sayeef Salahuddin,<sup>7</sup> Arthur F. Hebard,<sup>4</sup> Harold Y. Hwang,<sup>3,5</sup> and Ramamoorthy Ramesh<sup>1,2,8</sup>

<sup>1</sup>*Department of Physics, University of California, Berkeley, California 94720, USA*

<sup>2</sup>*Materials Science Division, Lawrence Berkeley National Laboratory, Berkeley, California 94720, USA*

<sup>3</sup>*Department of Advanced Materials Science, University of Tokyo, Kashiwa, Chiba, Japan*

<sup>4</sup>*Department of Physics, University of Florida, Gainesville, Florida 32611, USA*

<sup>5</sup>*Japan Science and Technology Agency, Kawaguchi, 332-0012, Japan*

<sup>6</sup>*Applied Science and Technology Graduate Group,*

*University of California, Berkeley, California 94720, USA*

<sup>7</sup>*Department of Electrical Engineering and Computer Science,*

*University of California, Berkeley, California 94720, USA*

<sup>8</sup>*Department of Materials Science and Engineering,*

*University of California, Berkeley, California 94720, USA*

(Dated: September 9, 2010)

Ionic crystals terminated at oppositely charged polar surfaces are inherently unstable and expected to undergo surface reconstructions to maintain electrostatic stability. Essentially, an electric field that arises between oppositely charged atomic planes gives rise to a built-in potential that diverges with thickness. Here we present evidence of such a built-in potential across polar  $\text{LaAlO}_3$  thin films grown on  $\text{SrTiO}_3$  substrates, a system well known for the electron gas that forms at the interface. By performing tunneling measurements between the electron gas and metallic electrodes on  $\text{LaAlO}_3$  we measure a built-in electric field across  $\text{LaAlO}_3$  of  $80.1 \text{ meV/\AA}$ . Additionally, capacitance measurements reveal the presence of an induced dipole moment across the heterostructure. We foresee use of the ionic built-in potential as an additional tuning parameter in both existing and novel device architectures, especially as atomic control of oxide interfaces gains widespread momentum.

As dictated by Maxwell's equations, the accumulation of screening charges at the boundary between dissimilar materials is one means<sup>1</sup> of ensuring a continuous electric displacement at the interface.<sup>2</sup> For instance, a layer of trapped screening charge forms the two dimensional electron gas that compensates a polarization mismatch at gallium nitride<sup>3</sup> and zinc oxide<sup>4</sup> based heterostructure interfaces. In insulating oxides, charge accumulation was observed at the interface between  $\text{SrTiO}_3$  substrates with atomically precise surfaces and polar  $\text{LaAlO}_3$  films.<sup>5</sup>  $\text{LaAlO}_3$  thin films grown on singly terminated  $\text{SrTiO}_3$  surfaces<sup>6</sup> comprise negatively charged  $\text{AlO}_2$  and positively charged  $\text{LaO}$  end planes and are polar in the ionic limit.<sup>1,7,8</sup> When at least four unit cells (u.c.) of  $\text{LaAlO}_3$  are deposited on  $\text{TiO}_2$  terminated  $\text{SrTiO}_3$ , an electron gas forms near the interface in  $\text{SrTiO}_3$ .<sup>5,9,10</sup> It is often hypothesized that at a thickness of four u.c. the potential across  $\text{LaAlO}_3$  exceeds the band gap of  $\text{SrTiO}_3$  and electrons tunnel from the valence band of  $\text{LaAlO}_3$  to the  $\text{SrTiO}_3$  potential well, completely diminishing the potential across  $\text{LaAlO}_3$ .<sup>11</sup> Thus within this picture, in the presence of an electron gas no field would be expected across the  $\text{LaAlO}_3$ . However, if all the charge carriers do not lie precisely at the interface or have an extrinsic (oxygen vacancies<sup>12</sup> or cation doping<sup>13</sup>) origin, the  $\text{LaAlO}_3$  potential will not be fully screened and can thus be probed.<sup>14</sup> Alternatively, the precise band alignment between the  $\text{LaAlO}_3$  and  $\text{SrTiO}_3$  will also determine the strength of the residual fields in the  $\text{LaAlO}_3$ .<sup>15</sup> Addressing this issue by determining the existence of an uncompensated built-in potential

in  $\text{LaAlO}_3$  is central to understanding the true nature of the polar  $\text{LaAlO}_3/\text{SrTiO}_3$  interface.

We probe the potential landscape across the  $\text{LaAlO}_3$  and the interface region in  $\text{SrTiO}_3$  by employing a typical metal-insulator-metal capacitor geometry such that the  $\text{LaAlO}_3$  thin films form the dielectric layer sandwiched between evaporated metallic electrodes and the electron gas, as depicted in Fig. 1a and described in Methods. A bias voltage is applied to the top metallic electrode while the electron gas is held at ground.

A typical current-voltage ( $JV$ ) curve measured between a Pt top electrode and the electron gas for an  $\text{LaAlO}_3$  thickness,  $d_{\text{LAO}}$ , of 20 u.c. is shown in Fig. 1b and overlaid with theoretical curves, as labeled. Similar rectifying  $JV$  curves were measured for nine different  $\text{LaAlO}_3$  films with  $d_{\text{LAO}}$  ranging from 5 to 40 u.c. Junctions thinner than  $d_{\text{LAO}} = 20$  u.c. are well described by tunneling between the metal electrode and electron gas for both positive (+V) and negative (−V) applied biases, as described in detail in Supplementary Section I (SSI). Figure 1b shows excellent agreement with the theoretically calculated curve (black) using Simmons' direct tunneling model for +V. For samples with  $d_{\text{LAO}} \geq 20$  u.c. however, an additional contribution from interband tunneling for negative applied bias must be included, as shown in Fig. 1b.

The inset in Fig. 1c shows a sampling of the  $JV$  curves for various  $d_{\text{LAO}}$  with emphasis on the negative bias region at 100 K. It is clear that for a given voltage the current does not decrease monotonically with  $d_{\text{LAO}}$ . The main panel of Fig. 1c shows  $J$  as a function of  $d_{\text{LAO}}$  (open

circles) at  $V = -0.1$  V for all samples, revealing a clear peak at 20 u.c. (7.56 nm). The same trend is observed at all temperatures at negative bias. The dark blue curve in Fig. 1c shows calculated values for  $J$  vs.  $d_{\text{LAO}}$  within the direct tunneling model (see SSI), which agrees well with the data for thicknesses below 20 u.c.

The sudden increase of tunneling current at  $d_{\text{LAO}} = 20$  u.c. seen in Fig. 1c can be understood by considering the polar nature of  $\text{LaAlO}_3$ . We recall that in the presence of a large enough electric field, Zener breakdown occurs in insulators and electrons tunnel from the valence to conduction band.<sup>16</sup> For materials with a built-in polar electric field, the internal potential grows with increasing thickness until it equals the bandgap at a critical thickness,  $d^{\text{cr}}$ , giving rise to a significant increase in tunneling current.<sup>17</sup> For  $\text{LaAlO}_3$  thin films deposited on  $\text{TiO}_2$  terminated  $\text{SrTiO}_3$ , in the absence of complete screening an ionic built-in potential normal to the interface, pointing away from the  $\text{SrTiO}_3$  is expected.<sup>7,11</sup> Figs. 2a and 2b illustrate zero bias band diagrams (black outline) where the band bending in  $\text{LaAlO}_3$  reflects the unscreened potential for thicknesses below (Fig. 2a) and near (Fig. 2b)  $d^{\text{cr}}$ .<sup>7,18,19</sup> In green, we also sketch the cases for small positive (+V) and negative (-V) applied biases. While precise band alignments are difficult to accurately predict in the presence of electronic reconstruction, Fig. 2 reflects the band diagrams inferred from our measurements (see SSI).<sup>15</sup>

The band diagrams shown in the upper half of Fig. 2 depict the tunneling of electrons from the  $\text{SrTiO}_3$  to the Pt electrode for small biases (+V). The lower half of Fig. 2a shows electrons tunneling from the metal into the  $\text{SrTiO}_3$  well (-V), as determined from the data shown in Fig. 1b. Above a critical  $\text{LaAlO}_3$  thickness,  $d^{\text{cr}}_{\text{LAO}}$ , we also expect electron tunneling across the  $\text{LaAlO}_3$  bandgap (Fig. 2b), via the valence states for applied bias  $V$  when:

$$qV \geq E_{g(\text{LAO})} - qV_{bi}. \quad (1)$$

Here  $E_{g(\text{LAO})}$  is the bandgap of  $\text{LaAlO}_3$  and  $V_{bi}$  is the net built-in potential across  $\text{LaAlO}_3$  including contributions from both the ionic built-in potential ( $V_i$ ) and contributions from the Pt and  $\text{SrTiO}_3$  work function difference ( $V_m$ ), so that  $V_{bi} = V_i + V_m$  (see also Supplementary Fig. 2). Using the diagram in Fig. 2b, the current density of electrons tunneling across the  $\text{LaAlO}_3$  bandgap was calculated for small biases within the WKB approximation<sup>16,17</sup> as shown in SSI, using

$$\Phi(d_{\text{LAO}}) = E_{g(\text{LAO})} - qE_{bi}d_{\text{LAO}} - qV + \epsilon \quad (2)$$

as the potential barrier height, where  $\epsilon$  is the total kinetic energy of the tunneling electrons,  $E_{bi}$  the effective built-in electric field in  $\text{LaAlO}_3$ , and  $V = -0.1$  V. We obtain the light blue curve shown in Fig. 1c, which is in excellent agreement with the data using  $E_{g(\text{LAO})} = 5.6$  eV for  $\text{LaAlO}_3$ .<sup>20</sup> In SSI, we also show simulations of the  $JV$  curves using a numerical approach which complements the analysis presented thus far. A two band

Hamiltonian that accounts for interband tunneling was simulated using the Non-Equilibrium Green's Function (NEGF) method. We find qualitatively that the rectification, current density values and the peak near 20 u.c. are reproduced in the presence of  $V_i$  across  $\text{LaAlO}_3$ .

A distinguishing feature of polar tunnel barriers is the low tunnel probability just below  $d^{\text{cr}}$ .<sup>17</sup> Our measurements (Fig. 2c) indicate that  $d^{\text{cr}}_{\text{LAO}}$  lies somewhere between 17 u.c. and 20 u.c., or roughly 18.5 u.c. when using Pt electrodes. Thus, using  $d^{\text{cr}}_{\text{LAO}} = 18.5$ ,  $a = 0.378$  nm<sup>21</sup> for the lattice constant of  $\text{LaAlO}_3$ , and  $E_{bi}d^{\text{cr}}_{\text{LAO}}a = qV_{bi} = E_{g(\text{LAO})} = 5.6$  eV (from Eq. 1 with  $qV = 0$ ), we obtain  $E_{bi} = 80.1$  meV/Å as an estimate for the net built-in electric field across  $\text{LaAlO}_3$ . Alternatively  $E_{bi} = 93.0$  meV/Å if the experimentally measured thin film value,<sup>22</sup>  $E_{g(\text{LAO})} = 6.5$  eV is used instead.  $E_{bi}$  reduces to 50.3 meV if tunneling from the  $\text{LaAlO}_3$  valence to the  $\text{SrTiO}_3$  conduction band is assumed instead, as discussed in SSI as an alternate scenario. Using the estimated (see SSI) chemical potential difference between Pt and the  $\text{SrTiO}_3$  ( $\approx 1.30$  eV giving 18.6 meV/Å for 18.5 u.c.) we arrive at 61.5 meV/Å for the  $V_i$  contribution across  $\text{LaAlO}_3$  using the 5.6 eV bandgap (or 74.4 meV/Å using  $E_{g(\text{LAO})} = 6.5$  eV). We note that band bending across the  $\text{LaAlO}_3$  resulting from the metal and  $\text{SrTiO}_3$  work function difference is thickness independent and thus cannot account for the observed thickness dependence (see Supplementary Fig. 2). It is not clear what fraction of the  $V_i$  is partially screened by the electron gas or partially compensated by covalency within the  $\text{LaAlO}_3$ .<sup>11,18</sup>

It is interesting to note that  $d^{\text{cr}}_{\text{LAO}} \approx 18.5$  u.c. for tunnel-coupling of the two  $\text{LaAlO}_3$  surfaces (in the presence of a Pt electrode) is close to the value of 15 u.c. (using no metal electrode) above which a drop in the in-plane mobility<sup>23</sup> and change in the in-plane magnetoresistance<sup>23,24</sup> have previously been observed.

Our data clearly reveal that the electron gas does not fully screen  $V_i$  across  $\text{LaAlO}_3$ . This suggests a few possibilities: (i) the charge carriers do not all lie exactly at the interface and are buried one or a few monolayers within the  $\text{SrTiO}_3$ , or (ii) the metal electrodes deposited on the  $\text{LaAlO}_3$  modify the band alignments and thus the carrier density of the electron gas. The latter effect may explain the failure to detect a built-in potential using photoemission experiments conducted in the absence of metal electrodes.<sup>10,15</sup> The present work cannot distinguish between the above two scenarios, both of which may be at play.

Uncompensated built-in potentials across ionic insulators ( $V_i$ ) are analogous to the built-in potentials that arise in semiconductors due to free charge separation and the switchable built-in potentials found in ferroelectrics, generally resulting from covalently bonded dipoles.  $V_i$  is most similar to the piezoelectric built-in potential in the wide bandgap polar III-V and II-VI wurzite semiconductor heterostructures.<sup>3,4,25</sup> However, the difference characterizing polar insulators such as  $\text{LaAlO}_3$  is the ionic origin of the built-in field, which is fundamentally different

from the piezoelectric fields in the wide bandgap semiconductors: The piezoelectric fields result from strain induced atomic displacements<sup>26</sup> while the ionic built-in fields are inherent to the layered, ionic structure of polar perovskite oxides and only arise in the presence of appropriate atomic terminations.<sup>8</sup> Unlike the polar semiconductors, atomic displacements work to cancel  $V_i$ .<sup>27</sup> In addition to the piezoelectric polarization, a spontaneous polarization that depends on surface termination also arises in wide band gap semiconductor heterostructures,<sup>26,28</sup> the analog of which, as discussed next, may also exist in the  $\text{LaAlO}_3/\text{SrTiO}_3$  system.

The  $\text{SrTiO}_3$  interface region can be probed by tuning both the charge density and the  $\text{SrTiO}_3$  dielectric permittivity,  $\chi_{STO}$ , with temperature and applied electric fields.<sup>12,29,30</sup> If the  $\text{LaAlO}_3/\text{SrTiO}_3$  heterostructure is compared to the inversion layer in a lightly doped metal-oxide-semiconductor (MOS) capacitor, we can expect changes in the charge density of the inversion layer as a function of temperature and gate voltage.<sup>31</sup> Alternatively, changes in  $\chi_{STO}$  may also tune an interface dipole layer in  $\text{SrTiO}_3$ .<sup>32-34</sup> Changes in either  $\chi_{STO}$  or the charge density will be reflected in the barrier height,  $\Phi$ , for electrons tunneling *from* the  $\text{SrTiO}_3$  potential well.

In order to probe changes in the barrier height, we tune  $\chi_{STO}$  and the charge density using both temperature and an applied field across  $\text{SrTiO}_3$ , and measure the resulting tunneling curves as shown in Figs. 3a and 3c respectively. We find that in the  $-V$  region where electrons are tunneling from the metal electrode via the  $\text{LaAlO}_3$  valence band *to* the  $\text{SrTiO}_3$  potential well,  $JV$  undergoes little change while significant changes are observed for electrons tunneling from the electron gas in  $\text{SrTiO}_3$  for  $+V$ .

Both the backgate and temperature dependence data are qualitatively in agreement with the simple barrier height change arguments presented above. Fig. 3b shows changes in  $J$  and  $\Phi$  as a function of temperature as obtained by fitting to the direct tunneling model (SS1). Here  $J \propto \exp^T$  which can be understood as follows, in terms of the charge density: As fewer states are occupied in the interface region with decreasing temperature, the barrier height of electrons tunneling from the  $\text{SrTiO}_3$  increases. Similarly, Fig. 3c shows  $JV$  for the 30 u.c. sample at 50 K for several back gate fields ( $E_{bg}$ ) applied with respect to the electron gas, as schematically depicted in the inset. Fig. 3d shows the corresponding changes in  $J$  and  $\Phi$ . We again find that  $J \propto \exp^{|E_{bg}|}$ . Here negative  $E_{bg}$  reduces the charge density and thus the tunneling current from the  $\text{SrTiO}_3$ . We do not observe significant changes in the  $\Phi$  for positive  $E_{bg}$  since the electron gas has a higher charge density.<sup>30</sup>

Alternatively, a change in the dipole strength<sup>32,33</sup> at the interface with temperature and an applied back gate will modify the band alignments (i.e.  $\Delta E_C$ ) and hence  $\Phi$ . Since  $\text{SrTiO}_3$  is an incipient ferroelectric and is sensitive to the slightest strain perturbation, it is possible that we are indeed observing the effects of an interface dipole.<sup>35</sup>

Capacitance measurements are an excellent tool for probing this latter notion. Fig. 4a shows  $CV$  measured between the metal electrode and electron gas at 10 K for a 30 u.c. sample. Details of the complex impedance analysis are discussed in Supplementary Section II, or SSII. Figure 4b shows the phase angle,  $\delta$ , of the complex impedance as a function of  $V$  at several temperatures.  $\delta$  is calculated to be exactly  $90^\circ$  for a perfect capacitor, becoming less than  $90^\circ$  as the dielectric becomes more conducting (SSII). As seen here, the drop off to zero in  $\delta(V)$  coincides with the sharp drop in  $CV$  in Fig. 4a and the onset of Zener tunneling. During Zener tunneling charge carriers are introduced into the  $\text{LaAlO}_3$  bandgap and  $\text{LaAlO}_3$  is no longer a good dielectric, behaving more like a resistor. When  $\delta = 90^\circ$  however, the system behaves like a metal-insulator-metal tunnel junction. For samples thinner than 20 u.c., while we do observe a typical MOS capacitor depletion capacitance at high enough negative bias, no corresponding drop in the complex phase angle is observed (SSII).

Figures 4b to 4d provide a closer examination of the hysteretic behavior that appears below 100 K in both the  $CV$  and  $\delta(V)$ . We find that the memory window defined by the hysteresis remains constant at  $\Delta V = 0.16$  V for frequencies below the  $RC$  roll off when  $V_{max} = 0.8$  V (Fig. 4b), and increases with decreasing temperature (Fig. 4c). The memory window also increases with increasing maximum applied voltage ( $V_{max}$  in Fig. 4d). The lack of a frequency dependence and decrease in hysteresis with increasing temperature rule out the role of interface traps which are more active at higher temperatures and have a characteristic time dependence associated with charging/discharging.<sup>31</sup>

The data however compare well to the response measured for metal-ferroelectric-insulator-metal or semiconductor (MFIM or MFIS) junctions.<sup>36,37</sup> Using the change in charge density for the high and low  $C$  values shown in Fig. 4a, we obtain  $18 \text{ nC/cm}^2$  as an estimate of the remnant polarization for a maximum applied voltage of 0.8 V. Given that ferroelectric behavior in  $\text{LaAlO}_3$  has never been observed and that the  $\text{SrTiO}_3$  is an incipient ferroelectric, any dipole switching can be attributed to a thin layer in  $\text{SrTiO}_3$  near the interface.<sup>38</sup> Although, we do note that recent theoretical models of the  $\text{LaAlO}_3/\text{SrTiO}_3$  system point to the possibility of ferroelectric-like distortions in the  $\text{LaAlO}_3$  layer as well.<sup>2,39,40</sup> In accord with previous observations however,<sup>38</sup> we suspect an interface dipole in  $\text{SrTiO}_3$ , which in turn suggests that the electron gas lies not exactly at the interface, but buried one or a few monolayers within the  $\text{SrTiO}_3$ . We thus speculate that the large influx of charge carriers into the potential well at the onset of Zener tunneling changes the local electric field and modifies the dipole strength, causing the observed hysteretic behaviour in  $CV$ .

These observations support recent experimental evidence of an induced polarization with bound charges in addition to free charge near the interface in  $\text{SrTiO}_3$ .<sup>41,42</sup>

Furthermore, there is evidence from both X-Ray<sup>43</sup> and TEM<sup>21</sup> measurements that when  $\text{LaAlO}_3$  with a 3% lattice mismatch is deposited on the (001)  $\text{SrTiO}_3$  substrates, distortions in the  $\text{TiO}_6$  octahedra occur at the interface. It is also well known that biaxial strain as well as a strain gradient can induce ferroelectric<sup>44</sup> and flexoelectric<sup>45</sup> polarizations in  $\text{SrTiO}_3$ . The resulting bound charges would give rise to a finite electric field and confining potential at the interface.<sup>27,46,47</sup> This is analogous to the mechanism that gives rise to a confined electron gas in wide bandgap polar GaN (III-V) and ZnO (II-VI) based heterostructures.<sup>3,4</sup> Thus the weak polarity of the  $\text{SrTiO}_3$  may also play an important role in determining the electrostatic boundary conditions at the  $\text{LaAlO}_3/\text{SrTiO}_3$  interface, in direct comparison with the polar semiconductors. Theoretical studies that account for the weak polarity of  $\text{SrTiO}_3$  predict a termination dependent electronic reconstruction even on bare  $\text{SrTiO}_3$  (001) substrates.<sup>48</sup>

The precise roles played by both  $\text{SrTiO}_3$  and  $\text{LaAlO}_3$  polarities in the electron gas formation remains an open question. This issue may gain clarity by further investigating the temperature and back gate dependence of the tunneling current (shown in Fig. 3) and in-plane transport across the electron gas. In general the presence of built-in and induced electric fields across the  $\text{LaAlO}_3/\text{SrTiO}_3$  heterojunction highlight its many similarities with polar wide-band gap semiconductor heterostructures. Despite the many open questions, the compelling analogies portend use of the polar insulator heterostructures as a new generation of systems for exploring mesoscopic phenomenon in confined electron gases, while addressing unresolved issues related to the origin of the interface conductivity. Furthermore, the electric fields intrinsic to polar ionic insulators may prove to be advantageous for immediate use in applications that benefit from enhanced built-in potentials, as already demonstrated with the polar semiconductors.<sup>49</sup> In fact, given their larger bandgaps, polar insulators hold the tantalizing possibility of attaining larger built-in potentials than those currently attainable. As semiconductor device concepts achieve maturity, much of the same

phenomenology can be translated to the complex oxides which offer many more degrees of freedom for exploration.

## Methods

The  $\text{LaAlO}_3/\text{SrTiO}_3$  samples used for this study were fabricated (in Kashiwa) by epitaxially depositing  $\text{LaAlO}_3$  films on  $\text{TiO}_2$  terminated (001)  $\text{SrTiO}_3$  substrates by pulsed laser deposition using a KrF laser. Before growth, the substrates were preannealed at 1223 K for 30 min in an oxygen environment of 0.67 mPa. Following this anneal the growth was performed at 1073 K in an oxygen pressure of 1.33 mPa, at a repetition rate of 2 Hz. The total laser energy was 20 mJ, and the laser was imaged to a rectangular spot of area approximately  $2.3 \times 1.3 \text{ mm}^2$  on the single crystal  $\text{LaAlO}_3$  target using an afocal zoom stage. After growth, the samples were cooled to room temperature in an  $\text{O}_2$  pressure of  $4 \times 10^4 \text{ Pa}$ , with a one hour pause at 873 K.<sup>9,30</sup> Nine samples with  $\text{LaAlO}_3$  thicknesses of 5, 7, 10, 13, 15, 17, 20, 30 and 40 u.c. were deposited in this way.

Several circular metallic electrodes with diameters ranging from 0.3 to 0.7 mm were thermally evaporated on each of the  $\text{LaAlO}_3$  films using a shadow mask. Au was used for the 30 u.c. sample and Pt for all other samples. The backgate was thermally evaporated onto the 30 u.c. sample. Gold wire (0.0025" gauge) was manually bonded to the electrodes using silver epoxy and an Al wirebonder was used to bond to the electron gas. The samples were cooled in (Quantum Design) PPMS and MPMS systems. Tunneling measurements were conducted in Kashiwa, Gainesville and Berkeley, using various electrometers and source-measure units, all giving the same results. Capacitance measurements were also performed in all three locations using (Hewlett-Packard) HP4284 LCR meters. For the back gate measurements, electric fields were applied in the following succession: 0 kV/cm  $\rightarrow$  negative fields  $\rightarrow$  positive fields.

---

\* Correspondence should be addressed to: [guneeta@berkeley.edu](mailto:guneeta@berkeley.edu)

<sup>1</sup> Goniakowski, J., Finocchi, F. & Noguera, C. Polarity of oxide surfaces and nanostructures. *Rep. Prog. Phys.* **71**, 016501 (2008).

<sup>2</sup> Stengel, M. & Vanderbilt, D. Berry-phase theory of polar discontinuities at oxide-oxide interfaces. *Phys. Rev. B* **80**, 241103 (2009).

<sup>3</sup> Ambacher, O. *et al.* Two-dimensional electron gases induced by spontaneous and piezoelectric polarization charges in N- and Ga-face AlGaN/GaN heterostructures. *J. Appl. Phys.* **85**, 3222–3233 (1999).

<sup>4</sup> Tsukazaki, A. *et al.* Quantum hall effect in polar oxide heterostructures. *Science* **315**, 1388–1391 (2007).

<sup>5</sup> Ohtomo, A. & Hwang, H. Y. A high-mobility electron gas at the  $\text{LaAlO}_3/\text{SrTiO}_3$  heterointerface. *Nature* **427**, 423–426 (2004).

<sup>6</sup> Kawasaki, M. *et al.* Atomic Control of the  $\text{SrTiO}_3$  Crystal Surface. *Science* **266**, 1540–1542 (1994).

<sup>7</sup> Nakagawa, N., Hwang, H. Y. & Muller, D. A. Why some interfaces cannot be sharp. *Nature Mater.* **5**, 204–209 (2006).

<sup>8</sup> Tasker, P. W. The stability of ionic crystal surfaces. *J. Phys. C: Sol. Stat. Phys.* **12**, 4977–4984 (1979).

<sup>9</sup> Thiel, S., Hammerl, G., Schmehl, A., Schneider, C. W. & Mannhart, J. Tunable Quasi-Two-Dimensional Electron Gases in Oxide Heterostructures. *Science* **313**, 1942–1945 (2006).

<sup>10</sup> Segal, Y., Ngai, J. H., Reiner, J. W., Walker, F. J. & Ahn,

- C. H. X-ray photoemission studies of the metal-insulator transition in  $\text{LaAlO}_3/\text{SrTiO}_3$  structures grown by molecular beam epitaxy. *Phys. Rev. B* **80**, 241107 (2009).
- <sup>11</sup> Pentcheva, R. & Pickett, W. E. Electronic phenomena at complex oxide interfaces: Insights from first principles. *J. Phys.: Condens. Mat.* **22**, 043001 (14pp) (2010).
  - <sup>12</sup> Siemons, W. *et al.* Origin of charge density at  $\text{LaAlO}_3$  on  $\text{SrTiO}_3$  heterointerfaces: Possibility of intrinsic doping. *Phys. Rev. Lett.* **98**, 196802 (2007).
  - <sup>13</sup> Willmott, P. R. *et al.* Structural basis for the conducting interface between  $\text{LaAlO}_3$  and  $\text{SrTiO}_3$ . *Phys. Rev. Lett.* **99**, 155502 (2007).
  - <sup>14</sup> Li, Y., Phattalung, S. N., Limpijumnong, S. & Yu, J. Oxygen-vacancy-induced charge carrier in n-type interface of  $\text{LaAlO}_3$  overlayer on  $\text{SrTiO}_3$ : Interface vs. bulk doping carrier (2009). arXiv:0912.4805v1.
  - <sup>15</sup> Gu, X., Elfimov, I. S. & Sawatzky, G. A. The role of the band gaps in reconstruction of polar surfaces and interfaces (2009). arXiv:0911.4145v1.
  - <sup>16</sup> Zener, C. A theory of electrical breakdown of solid dielectrics. *Proc. Roy. Soc. A* **145**, 523–529 (1934).
  - <sup>17</sup> Simon, J. *et al.* Polarization-induced Zener tunnel junctions in wide-band-gap heterostructures. *Phys. Rev. Lett.* **103**, 026801 (2009).
  - <sup>18</sup> Noguera, C. & Goniakowski, J. Polarity in oxide ultrathin films. *J. of Phys.: Cond. Matt.* (2008).
  - <sup>19</sup> Bykhovski, A., Gelmont, B., Shur, M. & Khan, A. Current-voltage characteristics of strained piezoelectric structures. *J. Appl. Phys.* **77**, 1616–1620 (1995).
  - <sup>20</sup> Lim, S. G. *et al.* Dielectric functions and optical bandgaps of high-K dielectrics for metal-oxide-semiconductor field-effect transistors by far ultraviolet spectroscopic ellipsometry. *J. Appl. Phys.* **91**, 4500–4505 (2002).
  - <sup>21</sup> Maurice, J.-L. *et al.* Electronic conductivity and structural distortion at the interface between insulators  $\text{SrTiO}_3$  and  $\text{LaAlO}_3$ . *Phys. Stat. Sol. (a)* **203**, 2209–2214 (2006).
  - <sup>22</sup> Mi, Y. Y. *et al.* Epitaxial  $\text{LaAlO}_3$  thin film on silicon: Structure and electronic properties. *Appl. Phys. Lett.* **90**, 181925 (2007).
  - <sup>23</sup> Bell, C., Harashima, S., Hikita, Y. & Hwang, H. Y. Thickness dependence of the mobility at the  $\text{LaAlO}_3/\text{SrTiO}_3$  interface. *Appl. Phys. Lett.* **94**, 222111 (2009).
  - <sup>24</sup> Brinkman, A. *et al.* Magnetic effects at the interface between non-magnetic oxides. *Nat. Mater.* **427**, 493–496 (2007).
  - <sup>25</sup> Simon, J., Protasenko, V., Lian, C., Xing, H. & Jena, D. Polarization-Induced Hole Doping in Wide-Band-Gap Uniaxial Semiconductor Heterostructures. *Science* **327**, 60–64 (2010).
  - <sup>26</sup> Yu, E. T. *et al.* Schottky barrier engineering in III–V nitrides via the piezoelectric effect. *Appl. Phys. Lett.* **73**, 1880–1882 (1998).
  - <sup>27</sup> Pentcheva, R. & Pickett, W. E. Ionic relaxation contribution to the electronic reconstruction at the n-type  $\text{LaAlO}_3/\text{SrTiO}_3$  interface. *Phys. Rev. B* **78**, 205106 (2008).
  - <sup>28</sup> Posternak, M., Baldeschi, A., Catellani, A. & Resta, R. Ab initio study of the spontaneous polarization of pyroelectric  $\text{BeO}$ . *Phys. Rev. Lett.* **64**, 1777–1780 (1990).
  - <sup>29</sup> Copie, O. *et al.* Towards two-dimensional metallic behavior at  $\text{LaAlO}_3/\text{SrTiO}_3$  interfaces. *Phys. Rev. Lett.* **102**, 216804 (2009).
  - <sup>30</sup> Bell, C. *et al.* Dominant mobility modulation by the electric field effect at the  $\text{LaAlO}_3/\text{SrTiO}_3$  interface. *Phys. Rev. Lett.* **103**, 226802 (2009).
  - <sup>31</sup> Sze, S. M. *Physics of Semiconductor Devices* (Wiley-Interscience, 2006), 3 edn.
  - <sup>32</sup> Susaki, T., Kozuka, Y., Tateyama, Y. & Hwang, H. Y. Temperature-dependent polarity reversal in  $\text{Au-Nb:SrTiO}_3$  Schottky junctions. *Phys. Rev. B* **76**, 155110 (2007).
  - <sup>33</sup> Hikita, Y., Nishikawa, M., Yajima, T. & Hwang, H. Y. Termination control of the interface dipole in  $\text{La}_{0.7}\text{Sr}_{0.3}\text{MnO}_3/\text{Nb:SrTiO}_3$  (001) schottky junctions. *Phys. Rev. B* **79**, 073101 (2009).
  - <sup>34</sup> Minohara, M., Yasuhara, R., Kumigashira, H. & Oshima, M. Termination layer dependence of schottky barrier height for  $\text{La}_{0.6}\text{Sr}_{0.4}\text{MnO}_3/\text{Nb:SrTiO}_3$  heterojunctions. *Phys. Rev. B* **81**, 235322 (2010).
  - <sup>35</sup> Müller, K. A. & Burkard, H.  $\text{SrTiO}_3$ : An intrinsic quantum paraelectric below 4 K. *Phys. Rev. B* **19**, 3593–3602 (1979).
  - <sup>36</sup> Liu, M., Kim, H. K. & Blachere, J. Lead-zirconate-titanate based metal/ferroelectric/insulator/semiconductor structure for nonvolatile memories. *J. Appl. Phys.* **91**, 5985–5996 (2002).
  - <sup>37</sup> Miller, S. L. & McWhorter, P. J. Physics of the ferroelectric nonvolatile memory field effect transistor. *J. Appl. Phys.* **72**, 5999–6010 (1992).
  - <sup>38</sup> Bickel, N., Schmidt, G., Heinz, K. & Müller, K. Ferroelectric relaxation of the  $\text{SrTiO}_3(100)$  surface. *Phys. Rev. Lett.* **62**, 2009–2011 (1989).
  - <sup>39</sup> Pentcheva, R. & Pickett, W. E. Avoiding the polarization catastrophe in  $\text{LaAlO}_3$  overlayers on  $\text{SrTiO}_3$  (001) through polar distortion. *Phys. Rev. Lett.* **102**, 107602 (2009).
  - <sup>40</sup> Bristowe, N. C., Artacho, E. & Littlewood, P. B. Oxide superlattices with alternating *p* and *n* interfaces. *Phys. Rev. B* **80**, 045425 (2009).
  - <sup>41</sup> Ogawa, N. *et al.* Enhanced lattice polarization in  $\text{SrTiO}_3/\text{LaAlO}_3$  superlattices measured using optical second-harmonic generation. *Phys. Rev. B* **80**, 081106 (2009).
  - <sup>42</sup> Salluzzo, M. *et al.* Orbital reconstruction and the two-dimensional electron gas at the  $\text{LaAlO}_3/\text{SrTiO}_3$  interface. *Phys. Rev. Lett.* **102**, 166804 (2009).
  - <sup>43</sup> Vonk, V. *et al.* Interface structure of  $\text{SrTiO}_3/\text{LaAlO}_3$  at elevated temperatures studied in situ by synchrotron X-rays. *Phys. Rev. B* **75**, 235417 (2007).
  - <sup>44</sup> Haeni, J. H. *et al.* Room-temperature ferroelectricity in strained  $\text{SrTiO}_3$ . *Science* **430**, 758–761 (2004).
  - <sup>45</sup> Zubko, P., Catalan, G., Buckley, A., Welche, P. R. L. & Scott, J. F. Strain-gradient-induced polarization in  $\text{SrTiO}_3$  single crystals. *Phys. Rev. Lett.* **99**, 167601 (2007).
  - <sup>46</sup> Yoshimatsu, K., Yasuhara, R., Kumigashira, H. & Oshima, M. Origin of metallic states at the heterointerface between the band insulators  $\text{LaAlO}_3$  and  $\text{SrTiO}_3$ . *Phys. Rev. Lett.* **101**, 026802 (2008).
  - <sup>47</sup> Glinchuk, M. D. & Morozovska, A. N. The internal electric field originating from the mismatch effect and its influence on ferroelectric thin film properties. *J. Phys.: Cond. Matt.* **16**, 3517–3531 (2004).
  - <sup>48</sup> Goniakowski, J. & Noguera, C. The concept of weak polarity: An application to the  $\text{SrTiO}_3$  (001) surface. *Surf. Sci.* **365** (1996).
  - <sup>49</sup> Cao, Y., Zimmermann, T., Xing, H. & Jena, D. Polarization-engineered removal of buffer leakage for GaN transistors. *Appl. Phys. Lett.* **96**, 042102 (2010).

## Acknowledgments

We thank J. H. Bardarson, M. Gajek and Prof. R. Dynes at UC Berkeley as well as X. Du at Stonybrook for discussions and comments on the manuscript. GSB acknowledges support from the Japan Society for Promotion of Science (Award No. SP08057) and the U.S. National Science Foundation (Award No. OISE0812816) as part of the 2008 E.A.P.S.I. fellowship program, under which this work was commenced. WS acknowledges support from the Dutch Organization for Scientific Research (NWO-Rubicon Grant). The work at Berkeley (RR) was supported by the U.S. Department of Energy under contract No. DE-AC02-05CH1123. The work at Florida (AFH) was supported by the U.S. National Science Foundation under Grant No. 0404962.

## Author Contributions

CB deposited the  $\text{LaAlO}_3$  films. GSB prepared and measured the tunnel junctions with CB, modeled the data with JR and analyzed the  $JV$  curves with JR and WS. SS simulated the  $JV$  curves within the NEGF approach. The manuscript was prepared by GSB with assistance/input from CB, JR, WS and YH. HYH, AFH and GSB contributed to conceptualizing the experiment. HYH provided insights and expertise on the  $\text{LaAlO}_3/\text{SrTiO}_3$  interface, RR on ferroelectricity and AFH on interpreting complex impedance.

## Competing Financial Interests

The authors declare no competing financial interests.

## Figure Legends

**Figure 1**

**Built-in polarization across  $\text{LaAlO}_3/\text{SrTiO}_3$  tunnel junction diodes | a,** Tunnel junctions are formed between thermally evaporated circular metallic electrodes on  $\text{LaAlO}_3$  and the electron gas, as described in Methods. **b,**  $JV$  curve measured at 10 K for a 20 u.c. sample compared to curves calculated within the direct and Zener tunneling models as labeled, and described in SSI. **c,**  $J$  vs.  $\text{LaAlO}_3$  thickness,  $d_{\text{LAO}}$ , for all samples at  $V = -0.1$  V showing a clear peak at 20 u.c. (7.56 nm). Calculated curves for direct tunneling (dark blue) and Zener tunneling (light blue) are labeled and shown. The inset provides a closer look at the negative bias region of  $JV$  for several thicknesses showing that  $J$  does not scale monotonically with thickness for a given  $V$  (see dotted line at  $V = -0.1$  V).

**Figure 2**

**Thickness dependent built-in potential and inter-band tunneling across polar  $\text{LaAlO}_3$  | a,** A schematic band diagram of the  $\text{LaAlO}_3/\text{SrTiO}_3$  interface at zero bias (black outline) for  $\text{LaAlO}_3$  thicknesses much less than the critical thickness,  $d_{\text{LAO}}^{\text{cr}}$ , for both small positive applied bias ( $+V$ , green outline on top sketch) and small negative applied bias ( $-V$ , green outline on bottom sketch). Unlike typical capacitors where bending across the dielectric is induced by the electrode work function difference alone,  $V_m$ , in  $\text{LaAlO}_3$  an *intrinsic* built-in potential,  $V_i$ , adds to the band bending. Following conventions used for the polar nitrides,<sup>19</sup> the bending in  $\text{LaAlO}_3$  reflects the ionic built-in potential as well as bending due to the Pt and  $\text{SrTiO}_3$  chemical potential difference, as described in detail in the text and in Supplementary Fig. 2. In treating the  $\text{LaAlO}_3$  as a wide bandgap insulator with a midgap Fermi level, we have not included any curvature that may appear in the  $\text{LaAlO}_3$  bands due to metal induced gap states. **b,** Our measurements suggest that at  $d_{\text{LAO}}^{\text{cr}}$ , the valence and conduction band of  $\text{LaAlO}_3$  align at the Fermi level giving rise to Zener tunneling across the  $\text{LaAlO}_3$  bandgap for  $-V$ . The band diagrams shown reflect this observation: The metal and electron gas remain pinned at the Fermi level while the potential across  $\text{LaAlO}_3$  increases with thickness. Given the excellent screening and small skin depth of Pt on the left, bending in the electrode is not shown and the band alignments give the appearance of changing. At the  $\text{SrTiO}_3/\text{LaAlO}_3$  interface, assuming the  $\text{SrTiO}_3$  is a semiconductor, a strong change in charge density is expected with increasing thickness but not observed,<sup>23</sup> and hence not shown. Thus, screening at the  $\text{LaAlO}_3/\text{SrTiO}_3$  interface may be aided by a dipole layer in  $\text{SrTiO}_3$ .<sup>33,34</sup> We also note that surface reconstructions, if present, add a degree of ambiguity to determining precise band alignments.<sup>15</sup> In SSI and Supplementary Fig. 2 we provide an in-depth discussion on thickness dependent band bending across  $\text{LaAlO}_3$  and the resulting band diagrams.

**Figure 3**

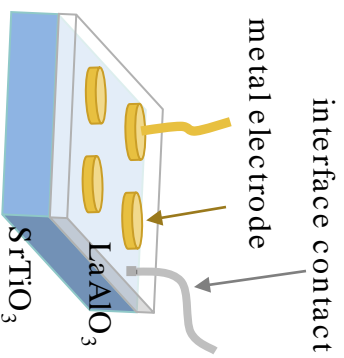
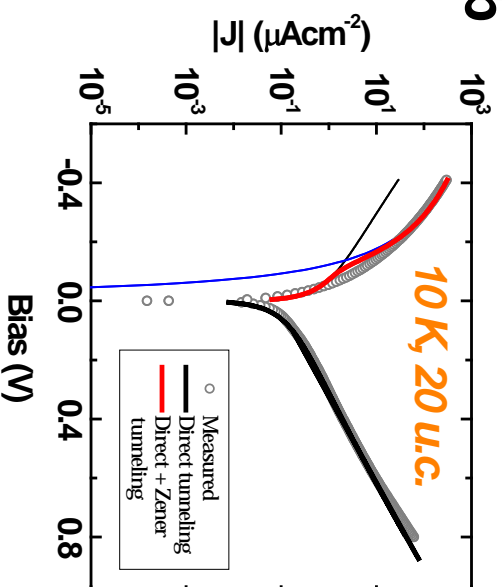
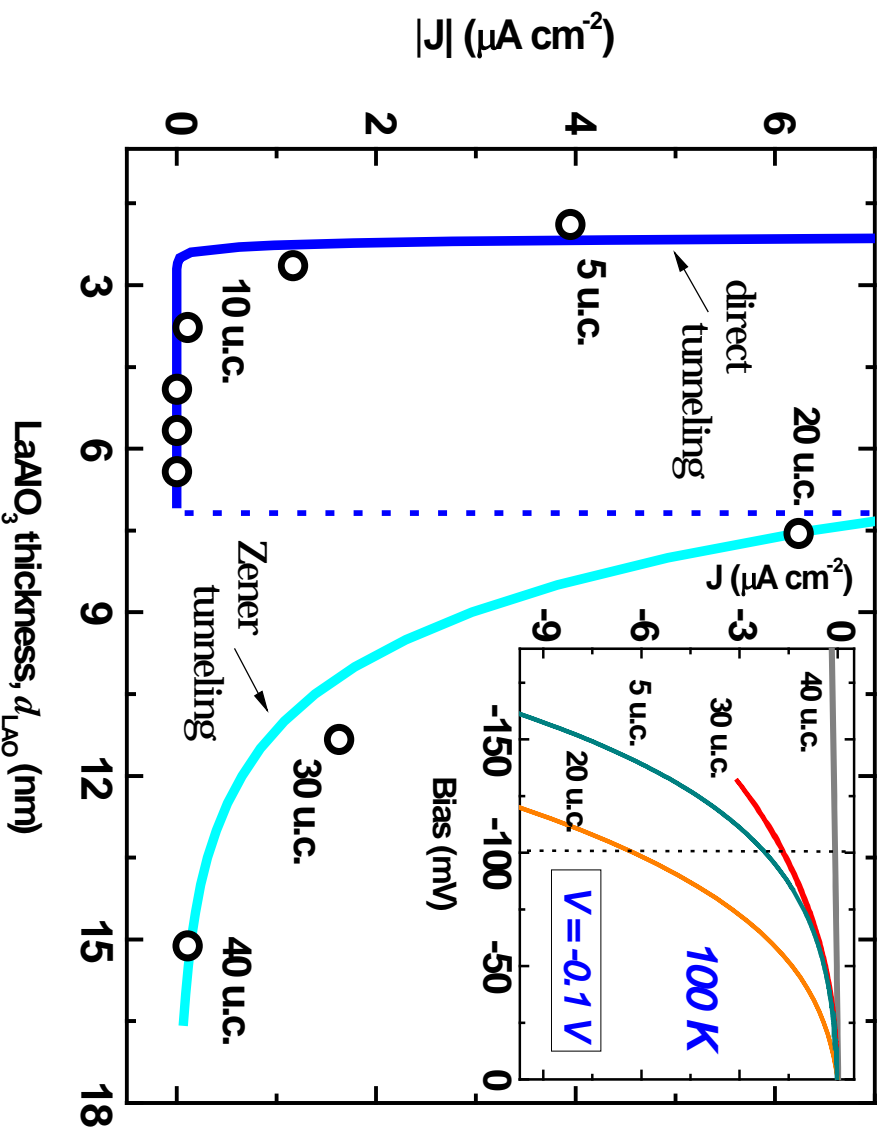
**Tuning the tunneling current across  $\text{LaAlO}_3$  by tuning the  $\text{SrTiO}_3$  permittivity and charge density | a,**  $JV$  curves for a 20 u.c.  $\text{LaAlO}_3$  sample are shown for several temperatures with theoretical fits to the direct tunneling model (black). The inset schematically depicts how changes in band bending in the  $\text{SrTiO}_3$  interface region produce changes in the barrier height  $\Phi$ . **b,**  $J$  and the barrier heights ( $\Phi$ ) extracted from fits to the direct tunneling model for each of the  $JV$  curves shown in **a** are shown as a function of temperature. Here  $J \propto \exp^T$ . **c,**  $JV$  for a 30 u.c.  $\text{LaAlO}_3$  at 50 K for several different positive and negative applied  $\text{SrTiO}_3$  back-gate fields,  $E_{bg}$ . The effect is much more pronounced for nega-

tive rather than positive biases, with  $J \propto \exp^{|E_{bg}|}$ . (The lowest point deviates from the linear trend likely since it is near measurement limits). **d**, Each of the  $JV$  curves shown in **c** was also fit to the direct tunneling model.  $\Phi$  increases linearly with increasingly negative backgate fields while  $J$  decreases logarithmically.

**Figure 4**

**Capacitance measurements agree with  $JV$  while also revealing an induced dipole across the heterostructure** | **a**,  $CV$  curves for a 30 u.c. sample measured at 10 K and 10 kHz are qualitatively similar to

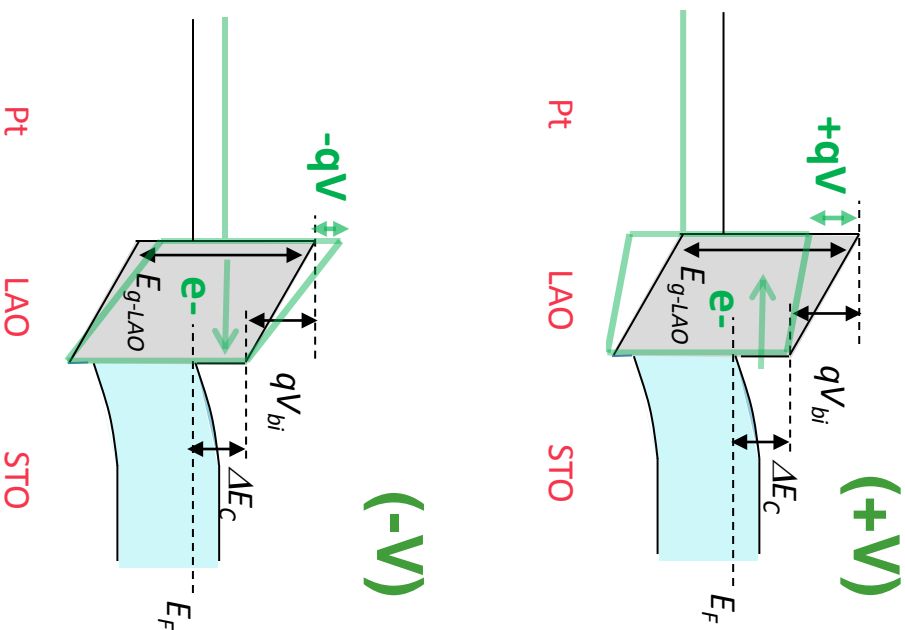
a metal-insulator-semiconductor (MIS) capacitor curves with a ferroelectric contribution, or a metal-insulator-ferroelectric-semiconductor (MIFS) capacitor. The drop in  $CV$  occurs during the Zener tunneling regime when carriers are introduced into the  $\text{LaAlO}_3$  bandgap, making it a leaky dielectric. **b**, The phase angle of the measured complex impedance as shown at several temperatures. A hysteresis appears near 100 K and increases with decreasing temperature. **c**, The hysteresis is frequency independent for frequencies below the  $RC$  roll-off limit, and **d**, the hysteresis window,  $\Delta V$ , increases with the maximum applied voltage,  $V_{max}$ , for a given sweep. **b** to **d** together qualitatively provide indications of dipole switching at the interface in  $\text{SrTiO}_3$ .

**a****b****c**



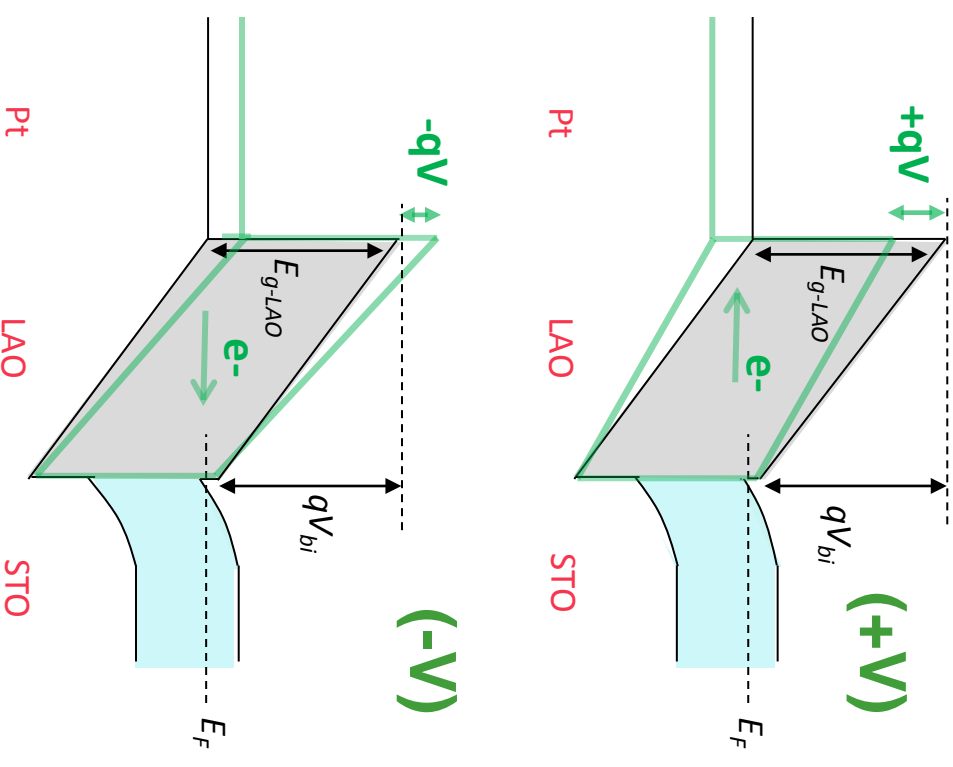
$$\underline{d_{LAO} < d_{LAO}^{cr}}$$

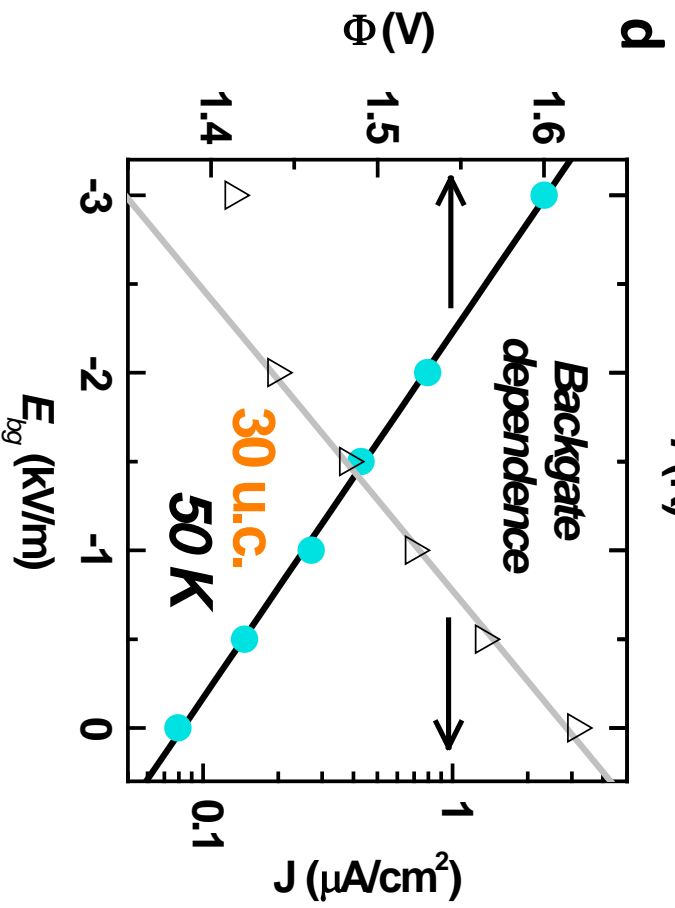
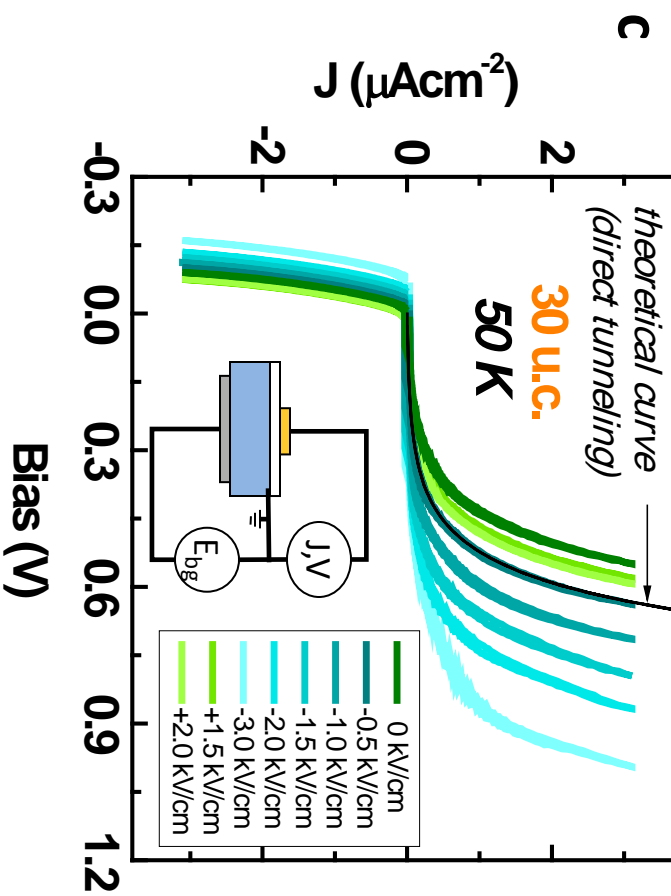
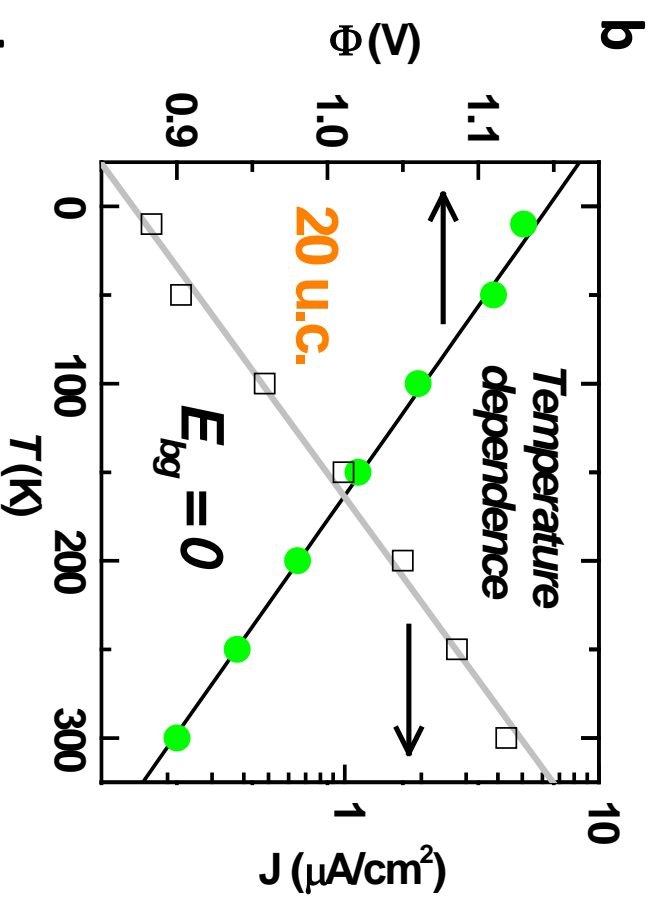
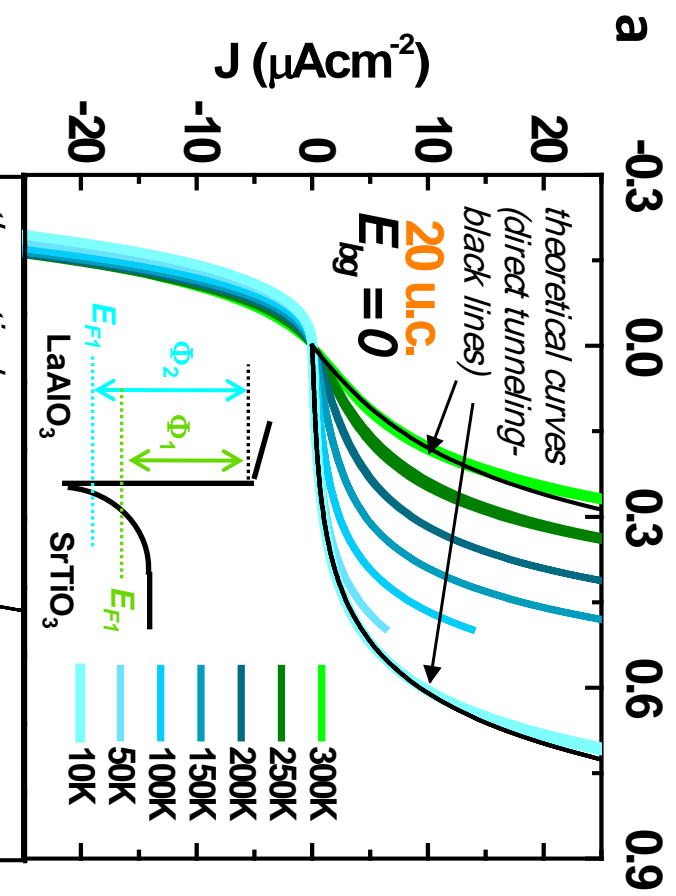
**a**

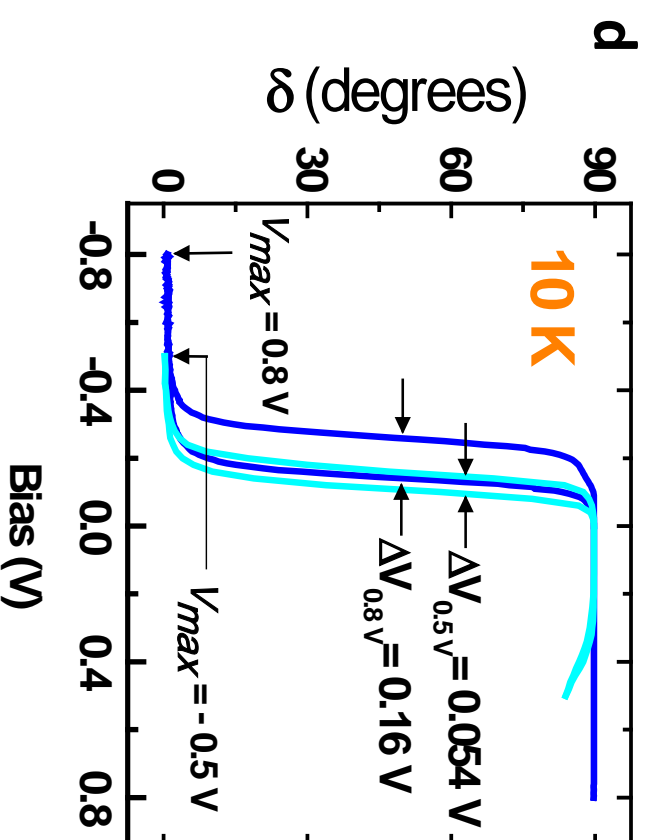
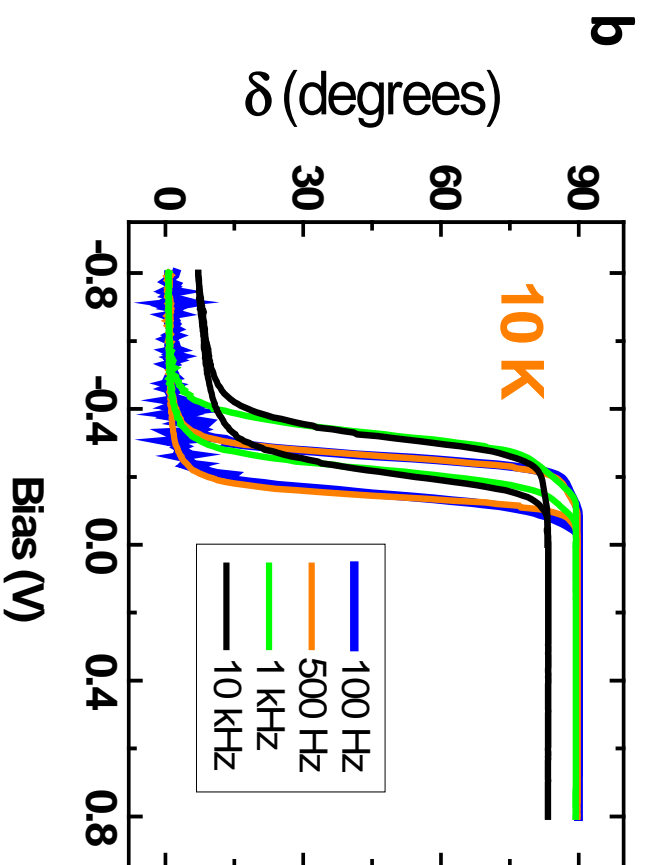
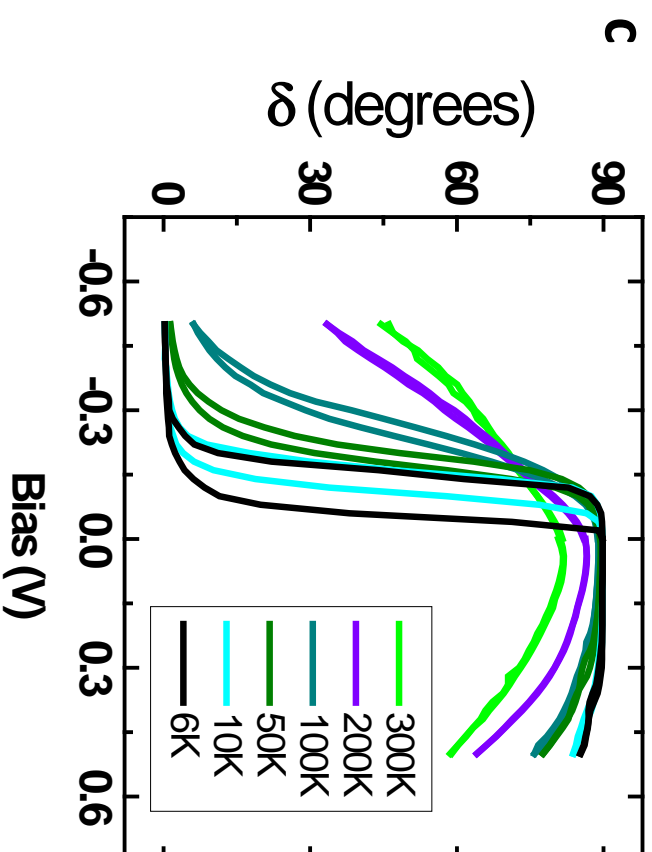
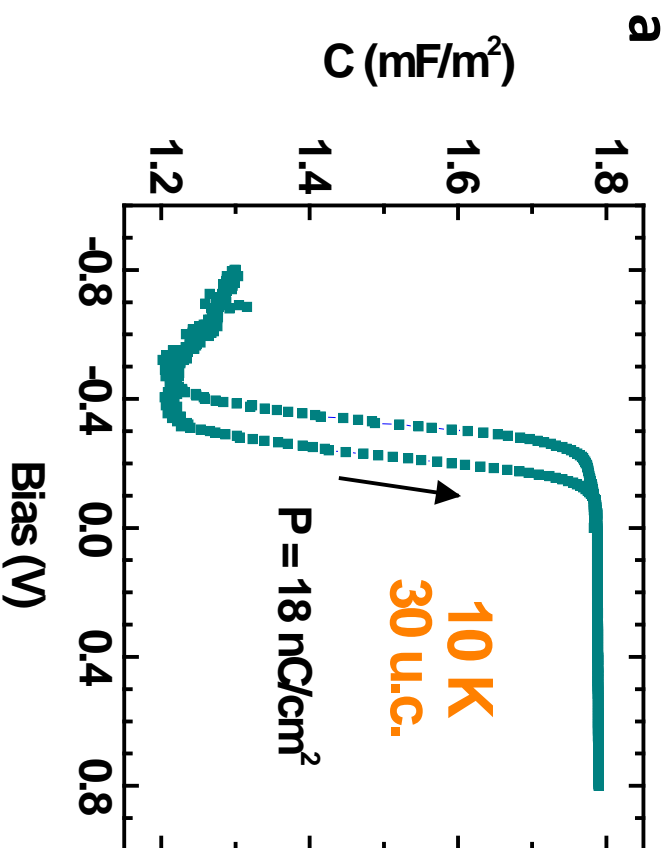


$$\underline{d_{LAO} \geq d_{LAO}^{cr}}$$

**b**







# Supplementary Information: Built-in and induced polarization across LaAlO<sub>3</sub>/SrTiO<sub>3</sub> heterojunctions

## Section I: Metal/LaAlO<sub>3</sub>/SrTiO<sub>3</sub> tunnel junctions

In order to identify the mechanisms governing the observed rectifying behavior in  $JV$  (see Fig. 1b of the main text), we have analyzed the data using standard semiconductor heterostructure and transport models, and have found tunneling between the metal electrode and the electron gas to be the predominant transport mechanism in the low voltage ranges studied in our work.

In the subsection labeled “Band diagram” below we give a description of the heterostructure band diagram and details on the material bandstructures considered for our work.

In accord with the band diagrams, the sub-section below on the “WKB tunneling models,” provides a description of the tunneling models used to understand the data presented in the main text.

Next, in the sub-section labeled “Discussion on tunneling models” we discuss the subtleties associated with our present model.

We also compare in-plane transport measurement with vertical transport across the heterostructure in the subsection labeled “Contact resistance and in-plane transport measurements”. We show that nearly all of the applied voltage drops across the heterostructure and is thus predominantly responsible for the observed effects.

Finally, we also simulate  $JV$  curves for the band diagrams shown in Supplementary Fig. 2 using the non-equilibrium Green’s function approach (NEGF). We qualitatively reproduce the observed rectification and thickness dependence as shown in the subsection, “Two band model simulations” below.

### Band diagram:

Supplementary Fig. 1 shows a sketch of the expected

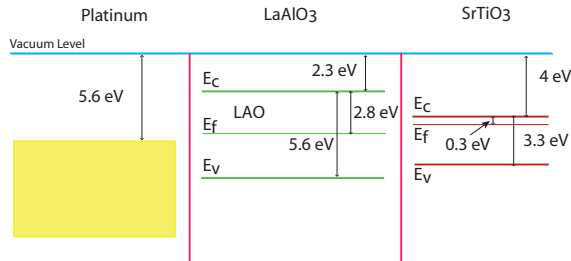


FIG. 1: Relative band alignments with respect to the vacuum level for each component of the Pt, LaAlO<sub>3</sub>, SrTiO<sub>3</sub> heterostructure. The Fermi level is shown as determined from measurements on bulk samples (see discussion in text), and prior to the three materials making contact.

band gaps and Fermi level  $E_f$  of each component of the tunnel junction as measured in bulk.<sup>1–5</sup> The Fermi level for SrTiO<sub>3</sub> is drawn at 0.3 eV below the conduction band rather than the midgap to account for oxygen vacancy doping in real substrates.<sup>2</sup> We note that for LaAlO<sub>3</sub> thin films grown on SrTiO<sub>3</sub>, a bandgap of 6.5 eV has also been measured<sup>6</sup> and will be compared with the 5.6 eV bulk gap<sup>4,5</sup> (depicted in Supplementary Fig. 1) using parenthesis in the analysis that follows. The 5.6 eV band gap in LaAlO<sub>3</sub> is a direct gap that forms at the  $\Gamma$ -point in  $k$ -space.<sup>4,5</sup> SrTiO<sub>3</sub> has an indirect band gap with a valence band edge maximum at the M-point and a conduction band minimum at the  $\Gamma$ -point.<sup>1</sup> Thus in an interband tunneling scenario between the LaAlO<sub>3</sub> valence band and either the LaAlO<sub>3</sub> or SrTiO<sub>3</sub> conduction bands, momentum is conserved along the  $\Gamma$ -point. For Pt, the K and X-points lie at the chemical potential.<sup>7</sup> When tunneling between the Pt top electrode and the SrTiO<sub>3</sub> electron gas, electronic transitions occur from the large metal Fermi surface of the Pt electrodes to various valley points of the SrTiO<sub>3</sub> conduction band.<sup>8</sup> Also, since the Pt electrodes were thermally evaporated and are thus not single crystalline or epitaxially matched with the (001) oriented LaAlO<sub>3</sub>, the wave vector will not always be conserved for electrons traversing the imperfect interface. Hence, tunneling between energetically available states of the Pt and SrTiO<sub>3</sub> will not be prohibited for states that lie at the same chemical potential but different points in  $k$ -space.<sup>8</sup>

While it is difficult to predict the exact band alignments in the presence of electronic reconstruction,<sup>9</sup> we sketch thickness dependent changes in the band alignments in Supplementary Fig. 2, as suggested by our experimental data (and expected for a material with an ionic built-in potential, analogous to ferroelectric insulators and the III-V nitrides<sup>10–12</sup>). The left most column of Supplementary Fig. 2 shows the expected band alignments in the absence of polarization in LaAlO<sub>3</sub>. In this case, the amount of band bending shown,  $V_m$ , will remain constant with thickness. The three sketches on the right show the band alignment of each material with respect to the vacuum level, for the case of a built-in potential in LaAlO<sub>3</sub>. Three different LaAlO<sub>3</sub> thicknesses are shown with the built-in potential, while directly below those sketches, the band alignments after contact are shown. We note that even the zero applied bias case has significant tilting across LaAlO<sub>3</sub> due to the built-in potential.<sup>10</sup> These six sketches in the right column clearly show that as the built-in potential changes across the LaAlO<sub>3</sub> with thickness, the alignment of the LaAlO<sub>3</sub> and SrTiO<sub>3</sub> conduction bands also gets modified.<sup>11</sup> If the band alignment did not change, the SrTiO<sub>3</sub> band would bend several eV below  $E_f$  giving rise to a significant increase in charge density, which is not observed.<sup>13</sup> This change in

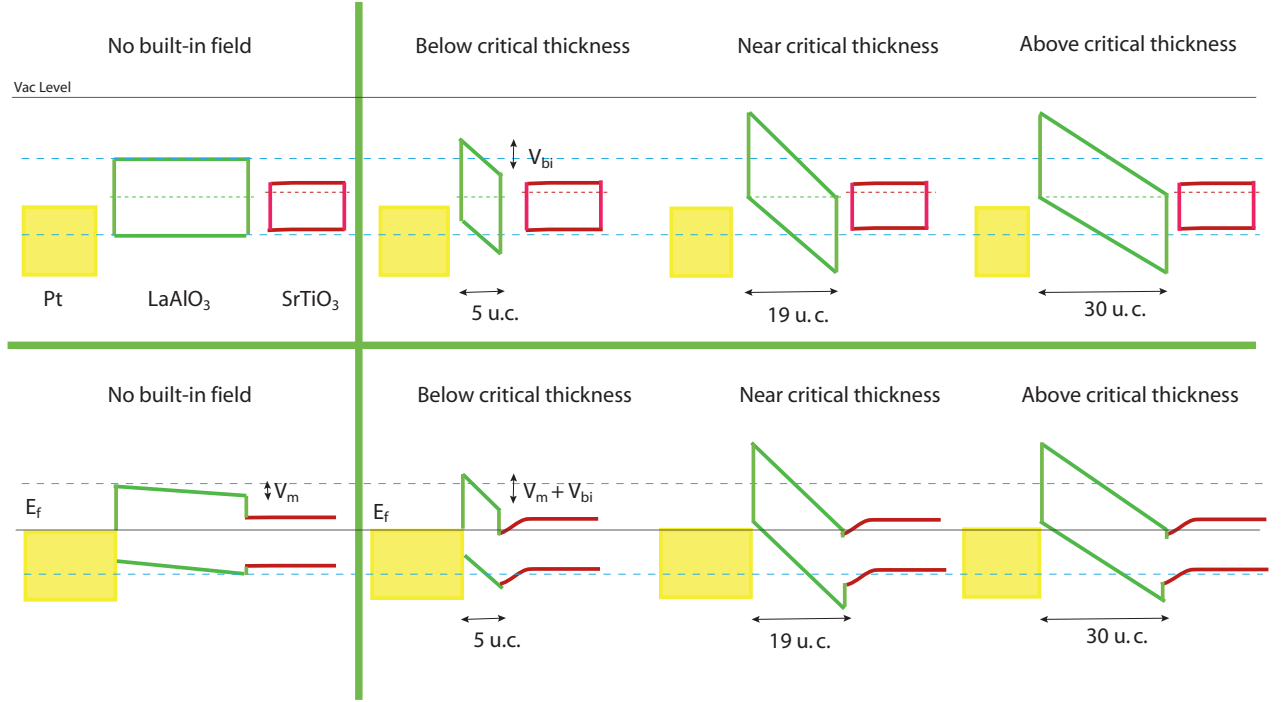


FIG. 2: Band alignments as inferred from our experimental data with and without the presence of a built-in potential in  $\text{LaAlO}_3$  are sketched. The top row shows vacuum level alignments for each component of the heterostructure. Dotted lines depict the  $\text{LaAlO}_3$  and  $\text{SrTiO}_3$  Fermi levels. Given its large bandgap,  $\text{LaAlO}_3$  is depicted as a good insulator with a midgap Fermi level. The bottom row shows alignments across the heterostructure after contact. **Left Column:** The column on the left shows the band alignments with respect to vacuum for no built-in potential in  $\text{LaAlO}_3$  (top row) and the band alignments after contact (bottom row). The difference between the Pt work function and  $\text{SrTiO}_3$  chemical potential give rise to thickness independent band bending  $V_m$  across  $\text{LaAlO}_3$ . Some curvature at the  $\text{LaAlO}_3/\text{SrTiO}_3$  interface may be present in this case as well, but is not shown. **Right Column:** The column on the right shows a series of three  $\text{LaAlO}_3$  thicknesses with an ionic built-in potential ( $V_i$ ) that is intrinsic to  $\text{LaAlO}_3$ .  $V_i$  increases with thickness (arising from a constant electric field in  $\text{LaAlO}_3$ ), and must thus also be included when the  $\text{LaAlO}_3$  is drawn as free standing in vacuum (top row). Bending across the  $\text{LaAlO}_3$  is assumed to be equal on either side of the midpoint which crosses the Fermi level.<sup>10</sup> The bottom row shows the band alignments of the heterostructure. The net built-in field across  $\text{LaAlO}_3$ ,  $V_{bi}$ , is the sum of the ionic contribution ( $V_i$ ) and the band bending caused by Pt and  $\text{SrTiO}_3$  ( $V_m$ ). It can be seen that either the  $\text{SrTiO}_3$  charge density gets modified with thickness or that the screening is aided by a surface dipole in  $\text{SrTiO}_3$ .<sup>14,15</sup> Previous experiments suggest that a significant charge in density modification can be ruled out.<sup>13</sup> Once the critical thickness is reached, the valence and conduction bands of  $\text{LaAlO}_3$  get pinned at the Fermi level since the maximum allowed built-in potential is equal to the bandgap. In actuality, there may be some additional curvature to the band bending or Fermi level pinning near the surface in  $\text{LaAlO}_3$ , which the present work cannot elucidate. As mentioned in the text, electronic reconstruction, if present, will add an additional degree of ambiguity to the band alignments.

band alignment may be manifest in an interface dipole layer in  $\text{SrTiO}_3$ , as observed in Schottky barriers with singly terminated  $\text{SrTiO}_3$  substrates,<sup>14,15</sup> and discussed in the main text. Given the unknowns, these details have not been included in the band diagram sketches. In the band diagram sketches we show the alignments as suggested by our data. For instance, the observation of Zener tunneling in itself suggests a particular band line up; specifically, one in which the metal, the  $\text{LaAlO}_3$  valence band, the  $\text{LaAlO}_3$  conduction band and the  $\text{SrTiO}_3$  potential well must be aligned at the Fermi level. The interface conductivity is represented by the presence of a notched potential well in  $\text{SrTiO}_3$  near the

interface with  $\text{LaAlO}_3$ .<sup>16</sup> We stress again that the electronic reconstruction scenario may modify this picture in unpredictable ways.<sup>9</sup> These uncertainties however do not affect our interband tunneling analysis which relies only on the  $\text{LaAlO}_3$  bandgap and built-in potential values.

#### WKB tunneling models:

Within the Wentzel-Kramers-Brillouin (WKB) approximation, the *transmission factor*<sup>8</sup> or the fraction of the probability current of electrons carried by the incident plane wave which passes through the tunneling barrier,  $\Phi(x)$  is, for a given thickness of  $\text{LaAlO}_3$ :

$$T_{wkb} = e^{-2 \int_0^{d_{\text{LAO}}} \sqrt{\frac{em^*}{\hbar^2} \Phi(x)} dx} \quad (1)$$

where  $x$  is the distance across the  $\text{LaAlO}_3$  thin film,  $d_{\text{LAO}}$  is the  $\text{LaAlO}_3$  thickness and  $m^*$  is the electron mass. This expression for  $T_{wkb}$  was derived by modeling the insulator as an infinite array of square potential wells.<sup>8</sup> Some assumptions implicit in the above equation with relevance to our heterostructure include (i) a negligible potential drop across the metal and the  $\text{SrTiO}_3$  and (ii) assuming that the transverse wave vectors are conserved across the heterostructure. The probability current as a function of the electron wave function,  $\Psi$ , is defined as

$$j = \frac{i\hbar}{2m} (\Psi \frac{\partial \Psi^*}{\partial x} - \Psi^* \frac{\partial \Psi}{\partial x}) \quad (2)$$

which gives the general expression for the tunneling current density, again, assuming conservation of the transverse wave vectors ( $k_t$ ):

$$J = \frac{2em^*}{(2\pi)^2 \hbar^3} \int_0^\infty dE_x [f_1 - f_2] \int \int T_{wkb} dE_t \quad (3)$$

where  $f_1$  and  $f_2$  are the Fermi functions for the metal on the left (1) and the right (2) of the insulator. The subscript  $t$  denotes the transverse direction while  $x$  is the direction perpendicular to the thin film plane. Neglecting the temperature dependence, within this WKB approximation, the following expression for the transmission factor was derived by J. Simmons<sup>17</sup> for tunneling across a metal-insulator-metal junction, using an average barrier height<sup>8</sup>,  $\bar{\phi}$ , to account for different metal work functions on either side of the barrier.

$$T_{wkb-Simmons} = e^{-\left(\frac{4\pi\beta d_{\text{LAO}}}{h}\right)(2m^*(\bar{\phi}-\epsilon))^{1/2}} \quad (4)$$

where  $\beta$  is an ideality factor (and is set to 1 for our purposes) and  $\epsilon$  is the kinetic energy in excess of the chemical potential. This leads to Simmons' basic direct tunneling (DT) expression:

$$J_{DT} = \frac{e}{2\pi\hbar(x\beta)^2} \times \left\{ \left(\bar{\phi} - \frac{eV}{2}\right) \exp\left[\frac{-4\pi\beta d_{\text{LAO}}(2m^*)^{1/2}}{h} \left(\bar{\phi} - \frac{eV}{2}\right)^{1/2}\right] - \left(\bar{\phi} + \frac{eV}{2}\right) \exp\left[\frac{-4\pi\beta d_{\text{LAO}}(2m^*)^{1/2}}{h} \left(\bar{\phi} + \frac{eV}{2}\right)^{1/2}\right] \right\}. \quad (5)$$

In Fig. 1c of the main text, we have simulated the exact form using  $\bar{\phi}=2.7$  eV (3.75 using  $E_{g(\text{LAO})} = 6.5$  eV), an average barrier height estimated from the band diagram shown in Fig. 2 for samples of thicknesses between 5 u.c. to 10 u.c., and obtain a value of  $0.60m_o$  ( $0.46m_o$  using  $E_{g(\text{LAO})} = 6.5$  eV) for the effective mass, which is about twice the value measured for MOS capacitors using  $\text{LaAlO}_3$  of  $0.27m_o$ .<sup>18</sup> Such a 50% change in effective mass has also been observed across ultra thin  $\text{SiO}_2$  tunnel barriers,<sup>19</sup> and given our assumptions for the average thickness as discussed next, we expect an uncertainty in

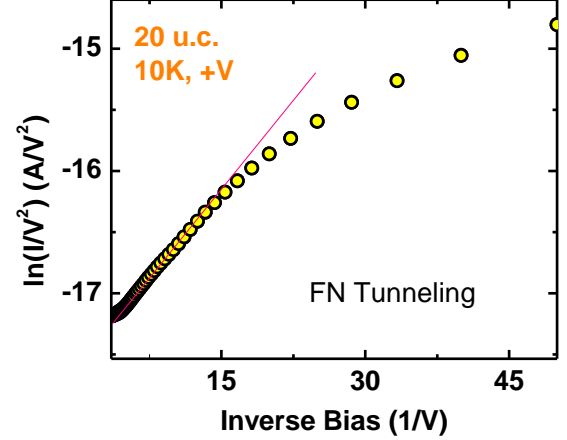


FIG. 3: For the higher positive applied voltages (+V), Fowler-Nordheim tunneling describes the data well for the 20 u.c. sample shown.

the effective mass value. The average value used for  $\bar{\phi}$  does not accurately account for the  $\text{LaAlO}_3$  built-in potential induced increase in barrier asymmetry with thickness. This feature of tunneling across a polar insulator is better captured using a numerical approach rather than the approximate Simmons' formula which only serves to qualitatively capture the essence of the transport across the heterojunction, confirming tunneling transport.

For the 20 u.c. sample shown in Fig. 1b on the other hand, it is necessary to use the reduced mass  $m_r^*$  for consistency with the Zener fits discussed below since tunneling may now also occur via the valence states. Significant barrier thinning and barrier height lowering due to the intrinsic  $\text{LaAlO}_3$  polarity, (shown in Fig. 1, main text) give  $\bar{\phi} = 1.55$  eV (1.23 eV for  $E_{g(\text{LAO})} = 6.5$  eV) at 10 K for +V using an effective mass of  $0.11m_o$  ( $0.14m_o$  for  $E_{g(\text{LAO})} = 6.5$  eV, both of which are found from the Zener tunneling fits in this thickness regime, as discussed further below). The respective barrier heights increase by  $\sim 0.01$  eV for thicker samples (see Fig. 3, main text). As shown in Fig. 1b, only a portion of the  $JV$  curve can be fit for negative applied bias ( $-V$ ). The fits to the remaining portion of the  $JV$  will be discussed below. Interestingly, unlike typical metal-insulator-metal tunnel junctions<sup>8</sup> where  $J \propto T^2$ , here we observe  $J \propto \exp(T)$  for positive biases down to 50 K (when tunneling from the  $\text{SrTiO}_3$  potential well, see Fig. 3b, main text), reflecting the similarities of this system to that of the inversion layer in a metal-oxide-semiconductor (MOS) capacitor which also exhibits temperature dependent tunneling currents.<sup>8,20</sup> Trap assisted tunneling also gives rise to a temperature dependence in tunnel junctions, however, we would expect to observe this for the  $-V$  region as well, which is not the case, as shown in the main text.

While we have hardly explored the effects of high applied bias on the tunnel junction (to avoid dielectric

breakdown), we expect that with a large enough field across  $\text{LaAlO}_3$ , the band bending will be strong enough such that electrons can tunnel from the metal to the conduction band of  $\text{LaAlO}_3$  for  $-V$  and, from the  $\text{SrTiO}_3$  potential well to the  $\text{LaAlO}_3$  conduction band for  $+V$ . In this case, the tunneling barrier shape is triangular and thus there is an effective barrier thickness reduction across  $\text{LaAlO}_3$  (similar to Zener tunneling), which is best described by the Fowler-Nordheim<sup>21</sup> (FN) equation:

$$J_{FN} = \frac{e^2 V^2}{16\pi^2 \hbar \phi d_{\text{LAO}}} \exp\left[\frac{-4\sqrt{2m^*} d_{\text{LAO}} (q\phi)^{3/2}}{3\hbar e V}\right]. \quad (6)$$

The FN plot in Supplementary Fig. 3 qualitatively shows that the high bias region for  $+V$  is indeed described by FN tunneling for 20 u.c.. This can also be seen in Fig. 1b. of the main text, where the data points begin to deviate from the direct tunneling fit at high biases. For most of our measurements, the high bias required to observe FN tunneling was not applied to avoid dielectric breakdown.

The peak in  $J$  at a critical thickness of 7.56 nm shown in Fig. 1c. of the main text can best be understood by considering interband tunneling as depicted in the band diagrams in Supplementary Fig. 2 and Fig. 2 in the main text. Alternate band alignment scenarios are discussed in the section labeled “Discussion on tunneling models,” but we note that all of the cases discussed require  $\text{LaAlO}_3$  to be polar with a critical thickness that aligns either (i) the  $\text{LaAlO}_3$  valence and conduction bands, (ii) the  $\text{LaAlO}_3$  valence band with the  $\text{SrTiO}_3$  conduction band or (iii) the metal with the  $\text{LaAlO}_3$  conduction band on the  $\text{SrTiO}_3$  side (i.e. triangular barrier). Thus the exact band alignment does not change our main result, that of polar  $\text{LaAlO}_3$ . However, as shown below, our analysis indicates interband tunneling is the likely scenario.

We obtain excellent fits to the data considering the first case of interband tunneling within the  $\text{LaAlO}_3$ . Interband tunneling current,  $J_Z$ , was first used to describe insulator breakdown by C. Zener<sup>22</sup> and calculated within the WKB approximation. The expressions for Zener’s volume generation rate of electrons from the valence band,  $n_Z$ , which can be used to obtain the current density,  $J_Z$ , and is given by:<sup>8,22</sup>

$$n_Z = \frac{eVa}{\hbar d_{\text{LAO}}} \exp\left[\frac{-\pi^2 m_Z^* a d_{\text{LAO}} E_{g(\text{LAO})}^2}{\hbar^2 eV}\right]$$

$$J_Z = \frac{en_Z W}{\tau} \quad (7)$$

Here  $a = 3 \times 10^{-8}$  cm is a constant and  $E_{g(\text{LAO})}$  is the  $\text{LaAlO}_3$  bandgap,  $W$  is the thickness (perpendicular the film plane) of the  $\text{LaAlO}_3$  valence band portion above the Fermi level and  $\tau$  is the carrier lifetime for electrons tunneling across the  $\text{LaAlO}_3$ . A number of modifications<sup>8</sup> to Zener’s original derivation give different prefactors for

$n_Z$  above, while the basic functional form remains the same, i.e.  $n_Z \propto V \exp(-1/V)$ . We find that the  $JV$  curve shown in Fig. 1b of the main text is well described by Eqn. 7 for  $-V$ , as shown. While Zener’s formulation describes the basic  $JV$  trend for an interband tunneling scenario, like the Simmons’ formula, it does not account for a built-in potential that grows with thickness. Thus, we turn to recent work on modeling thickness dependent Zener tunneling across polar AlN. In this work, Simon and coauthors simplify Eqn. 3 for small biases and approximate that:<sup>12</sup>

$$J_Z \approx \frac{e^3 m_Z^* T_{wkb} V^2}{4\pi^2 \hbar}. \quad (8)$$

Here the thickness dependence comes in via  $T_{wkb}$  which is the given by Eqn. 1 with  $\Phi(x)$  given by

$$\Phi(x) = E_{g(\text{LAO})} - qE_{bi}x + \epsilon = E_{g(\text{LAO})} \left(1 - \frac{qx}{d_{\text{LAO}}^{cr}}\right) + \epsilon \quad (9)$$

where  $x = d_{\text{LAO}}$ .  $\epsilon$  is the energy of the tunneling electrons,  $d_{\text{LAO}}^{cr}$  is the critical thickness from Fig. 2b in the main text and  $E_{bi} = E_{g(\text{LAO})}/d_{\text{LAO}}^{cr}$ , the effective built in electric field in  $\text{LaAlO}_3$ .

Using  $E_{g(\text{LAO})} = 5.6$  eV and  $d_{\text{LAO}}^{cr} = 18.5$  u.c. from the main text, we obtain a value of  $m_Z^* = 0.11m_o$  for the reduced  $\text{LaAlO}_3$  effective mass. The calculated curve for  $J_Z$  vs.  $d_{\text{LAO}}$  is shown on the right in Fig. 1c in light blue, and is in excellent agreement with the data. On the other hand, using the reported thin film  $\text{LaAlO}_3$  bandgap of 6.5 eV gives  $m_Z^* = 0.14m_o$ , for a calculated curve nearly identical to the one shown in Fig. 1c of the main text.

In Zener tunneling models, the reduced mass is an average of the light hole ( $m_h$ ) and electron ( $m_e$ ) masses. Our values of  $m_Z^* = 0.11m_o$  and  $0.14m_o$  are about a factor of two smaller than the value of  $0.27m_o$  found in the literature for metal to semiconductor tunneling in MOS capacitors fabricated using  $\text{LaAlO}_3$  as the dielectric.<sup>18</sup> This seeming discrepancy can be explained as follows: The effective mass (in the absence of manybody effects) is roughly given by  $m^* \sim \frac{E_{g(\text{LAO})}}{20} m_o$ .<sup>23,24</sup> Using  $E_{g(\text{LAO})} = 5.6$  eV as the lower bound for  $\text{LaAlO}_3$ , this gives  $0.28m_o$ , which is nearly equal to the value reported in the literature,  $0.27m_o$ .<sup>18</sup> For interband tunneling however, the reduced mass  $m_Z^* = m_r^*$  must be used, which is an average of the electron and light hole masses:  $\frac{1}{m_r^*} = \frac{1}{m_h} + \frac{1}{m_e}$ , or roughly about half of the effective mass,  $m_r^* \approx m^*/2 = 0.14m_o$  using the 5.6 eV bandgaps. When using the 6.5 eV bandgap,  $m_r^* \leq m^*/2 = 0.16m_o$ . Interestingly, the values we obtain from the simulated curves for the  $m_Z^*$ ,  $0.11m_o$  (using 5.6 eV) and  $0.14m_o$  (using 6.5 eV), within 80% of the expected values,  $0.14m_o$  (using 5.6 eV) and  $0.16m_o$  (using 6.5 eV).

#### Discussion on tunneling models:

Given that it is not clear from our measurements what, if any role the electronic reconstruction plays, a certain level of ambiguity remains in the band alignments considered in Fig. 2 of the main text and Supplementary



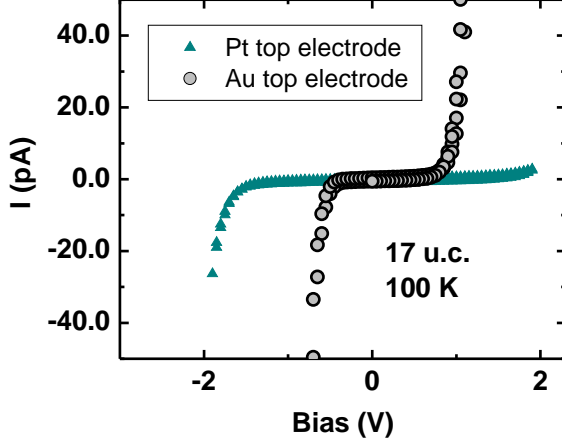


FIG. 4:  $IV$  curves for a 17 u.c. sample using Pt and Au electrodes with the same area. Higher currents are measured when using a metal (Au) with a lower work function than Pt.

Fig. 2. Thus it is possible that the sharp  $J$  peak observed in Fig. 1c is due to the  $\text{LaAlO}_3$  valence band aligning to the  $\text{SrTiO}_3$  conduction band instead, or the metal on the left of  $\text{LaAlO}_3$  aligning with the  $\text{LaAlO}_3$  conduction band on the right (across a triangular barrier). However, as noted earlier, we stress that regardless of the source of electrons during the tunneling process in Fig. 1c, the fact that a sudden increase in current density is observed above a critical thickness is indicative of a built-in potential across  $\text{LaAlO}_3$  that grows with thickness. In any of these cases, the desired band alignment occurs at the critical thickness, giving rise to a sharp increase in current. Our main conclusion is the same for any of the tunneling scenarios mentioned above.

Also, from our measurements, we cannot accurately confirm that the built-in potential grows exactly linearly with thickness up to 20 u.c. Accurate determination of this fact is well beyond the scope of this present work and the measurement techniques used here. Given the large bandgap of  $\text{LaAlO}_3$  we have also assumed no Fermi level pinning due to charge in the  $\text{LaAlO}_3$ . If however there is charge in or at the edge of the  $\text{LaAlO}_3$  (i.e. due to excessive band bending, etc), more complicated band diagrams will arise than the ones discussed here. Further experiments with other probes and numerical modeling are needed to understand this. Another caveat is the fact that our measurements have been conducted at relatively low biases to avoid damaging our ultra thin films. It is possible that conduction under high bias is better described by transport mechanisms not considered here or other effects in the  $\text{SrTiO}_3$  electron gas. While we have presented a model that captures the general observations, more rigorous numerical calculations and other experimental probes are needed for a full understanding of the  $\text{LaAlO}_3/\text{SrTiO}_3$  band structure and band alignments.

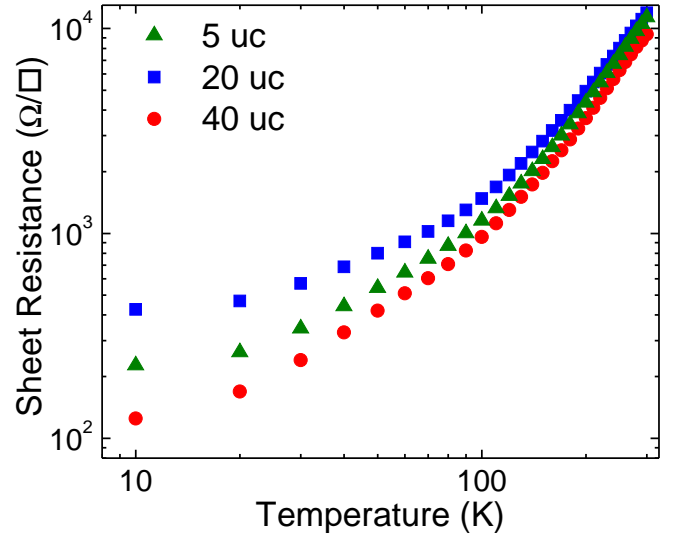


FIG. 5: Sheet resistance,  $R_s$ , as a function of temperature is shown for three sample thicknesses: the maximum (40 u.c.), minimum (5 u.c.) and a middle thickness (20 u.c.) used in our study. Measurements were performed on the same samples for which data are shown in the main text.

As a final note, we point out that in the simulations shown in Fig. 1c of the main text, all samples employ Pt electrodes while the 30 u.c. sample employs an Au electrode, as noted in the Methods section. This may explain why  $J$  is slightly higher than the theoretically calculated value for 30 u.c. in Fig. 1c of the main text, since Au has a lower work function than Pt.

#### Metal work function dependence:

As noted in the main text, depending on the relative value with respect to the  $\text{LaAlO}_3$  Fermi level, the metal work function will modify the net  $\text{LaAlO}_3$  built-in potential which adds to or subtracts from the ionic built-in potential. The difference in current densities between a tunnel junction with an Au vs. Pt electrode are shown in Supplementary Fig. 4.

#### Contact resistance and in-plane transport measurements

To ensure that most of the voltage drop in the metal- $\text{LaAlO}_3$ - $\text{SrTiO}_3$  junction occurs across the heterostructure and not the electron gas, we have also measured the in-plane sheet resistance of the samples. Three sample curves are shown in Fig. 5 for samples in the low, middle and high thickness ranges of Fig. 1c in the main text. More resistivity data on  $\text{LaAlO}_3/\text{SrTiO}_3$  interfaces fabricated under the same conditions can be found in Ref [5].<sup>13</sup>

Fig. 1c in the main text reveals that the lowest vertical resistivity occurs for the 20 u.c. thickness. In this case, for an applied  $V = -0.1$  V (electric field,  $E = V/d_{\text{LAO}} = 132$  kV/cm) at 100 K, we measure a current density of  $J = 6.23 \mu\text{A}/\text{cm}^2$ , which in turn gives a junction resistivity,  $\rho_{\perp} = 21.2 \text{ G}\Omega\text{-cm}$ . In comparison, the in-plane resistivity of the 20 u.c. sample at 100 K can be estimated



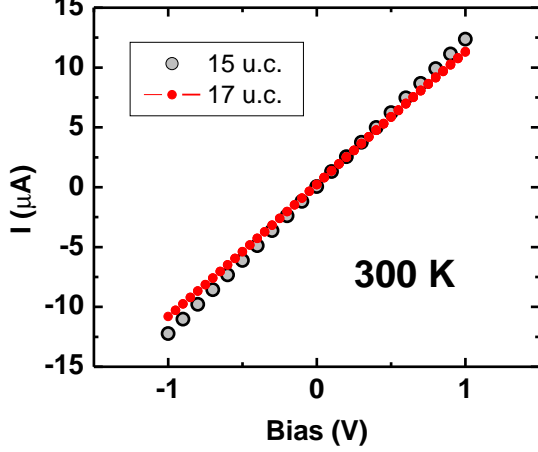


FIG. 6:  $IV$  measured between two wire-bonded contacts on a 15 u.c. and a 17 u.c. thick sample at room temperature. Such linear  $IV$  curves were measured on all samples to ensure metallic contacts to the electron gas.

from the sheet resistance,  $R_s$ , shown in Fig. 5, which is  $\approx 1.5 \text{ k}\Omega/\square$ . The in-plane resistivity is given by  $\rho_{||} = tR_s$ , where  $t$  is the electron gas thickness estimated to be between 7 and 15 nm,<sup>25</sup> for which the upper limit can then be estimated using the 15 nm thickness, giving,  $\rho_{||} = 2.25 \text{ m}\Omega\text{-cm}$ . Thus, we have  $\rho_{\perp} \approx \rho_{||} \times 10^9$  for the most conducting heterojunction at 100 K under a -0.1 V applied bias.

Using  $R_s$ , we can also estimate the voltage drop in the electron gas plane ( $V_{||}$ ) for the 20 u.c. sample at 100 K. In this case  $V_{||} = JAR_s$  where  $A = 0.3217 \text{ mm}^2$  is the electrode area and  $J = 6.23 \text{ }\mu\text{A}/\text{cm}^2$  when a total voltage of -0.1 V is applied across the sample. Using  $R_s$  for the resistance across the  $5 \text{ mm} \times 5 \text{ mm}$  square, we obtain  $V_{||} \approx 30 \text{ }\mu\text{V}$ . This is four orders of magnitude smaller than the total voltage drop across both the junction and the electron gas, 0.1 V. Thus, in this case, 99.97% of the voltage drop occurs across the heterostructure. The remaining samples, which are more insulating than the 20 u.c. sample, will have an even larger percentage of the voltage drop occurring across the heterostructure.

Additionally,  $JV$  curves between two contacts to the electron gas at approximately the diagonals of each  $5 \text{ mm} \times 5 \text{ mm}$  sample were measured to ensure linearity. See Supplementary Fig. 6 and compare to Supplementary Fig. 4. As can be seen, the in-plane currents are nearly six orders of magnitude higher than the vertical transport currents. Fig. 4 also demonstrates ohmic contacts to the electron gas. Overall, our in-plane vs. vertical measurement analysis ensures that the electron gas is not the source of the observed rectifying  $JV$  or the thickness dependence.

#### Two-band model simulations:

To compliment the analytical tunneling model used to describe the transport across the  $\text{LaAlO}_3/\text{SrTiO}_3$  het-

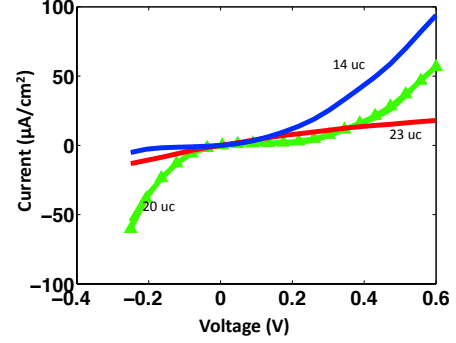


FIG. 7: Two band calculations reveal qualitative agreement with measured data shown in Fig. 1c of the main text: 1) The observed rectifying behavior is reproduced, 2) the same current value range is reproduced, and 3) the observed thickness dependence is reproduced.

erostructure, we use a simple numerical approach to simulate  $JV$  curves across the band diagrams shown in Supplementary Figs. 1 and 2.

Current voltage characteristics were calculated using the so called Keldysh formalism within the Non Equilibrium Green's Function approach (NEGF).<sup>26</sup> A two band Hamiltonian was set up where the band gap and effective mass of the conduction band and valence bands can be used as input parameters. The advantage of using such a two-band model is the fact that any interband-tunneling process is automatically included. Finally a real space Hamiltonian was formed assuming nearest neighbor coupling. To set up the electrostatic profile, a built in field  $E_{bi}$  was assumed to be present across  $\text{LaAlO}_3$ . Furthermore, a band offset  $\Delta E_c$  was assumed at the  $\text{LaAlO}_3/\text{SrTiO}_3$  interface. 1D electronic transport was calculated by solving for the Green's function assuming infinite leads where the lead self-energies were calculated in a recursive fashion following a modified Sancho-Rubio approach.<sup>27</sup> Finally, the the total current was calculated by summing over the modes in the transverse directions.

Fig. 7 shows the calculated  $JV$  for various thicknesses of the LAO layer. For this we have used a bandgap of  $E_{g(\text{LAO})} = 6.5 \text{ eV}$  rather than the bulk value of 5.6 eV, a conduction band offset  $\Delta E_c = 3.3 \text{ eV}$  and a built in electric field  $E_{bi} \equiv 0.9 \text{ V/nm}$ , corresponding to the band diagrams shown in Supplementary Figs. 1 and 2. The  $\text{SrTiO}_3$  was modeled as a wide bandgap semiconductor. Band profiles similar to those shown in Supplementary Figs. 1 and 2 were used as an input for various thicknesses. For consistency with the tunneling model fits, the effective mass was chosen to be  $0.14m_o$ . In addition, since applied voltages are much smaller than the internal

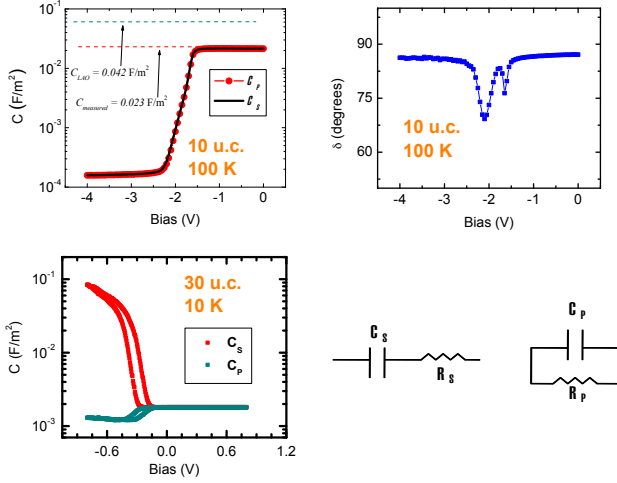


FIG. 8: **a**, shows both  $C_P$  and  $C_S$  for the 10 u.c. sample. The ideal and measured capacitance across the  $\text{LaAlO}_3$  are labeled. **b**, Complex phase angle for the 10 u.c. sample. **c**,  $C_P$  and  $C_S$  for a 30 u.c. sample.  $C_P$  is also shown in Fig. 4a, main text. **d** Circuit diagram for the parallel and series complex impedance model.

energy scales (e.g. band-gap, built-in voltage etc), charge self-consistency was ignored.

The calculated  $JV$  show asymmetric behavior qualitatively reproducing the features obtained in the experiment. The local density of states confirms direct tunneling in the forward bias ( $+V$ ) and interband tunneling in the reverse bias region ( $-V$ ). The results also reproduce the intriguing thickness dependence of the reverse bias ( $-V$ ) current (with a maximum current density measured for the 20 u.c.). Although no particular effort was made to optimize the parameters to exactly fit the experiment, the chosen set of parameters reproduce the values of the current in the same quantitative range as obtained in the experiment. A more rigorous analysis will require a self-consistent evolution of the band profile as the thickness is changed.

## Section II. Capacitance measurements across metal/ $\text{LaAlO}_3$ / $\text{SrTiO}_3$ tunnel junctions

Capacitance measurements are often ambiguous and complicated by the fact that commercial capacitance bridges compare the measured complex impedance to either a series or parallel resistor-capacitor model shown at the bottom right of Supplementary Fig. 8. For an *ideal* capacitor the series resistance (contact resistance)  $R_S$  is negligible while the parallel resistance (dielectric resistance)  $R_P$  is very large, and the measured capacitance is model independent (both  $R_P$  and  $R_S$  can be ignored). Hence  $C_P = C_S$  for an ideal capacitor and the measured phase angle ( $\delta$ ) of the complex impedance will be  $\delta = 90^\circ$ .

Supplementary Fig. 8a shows capacitance-voltage or

$CV$  curves measured for a 10 u.c. sample, which is typical for samples with thicknesses below 20 u.c.. Supple-

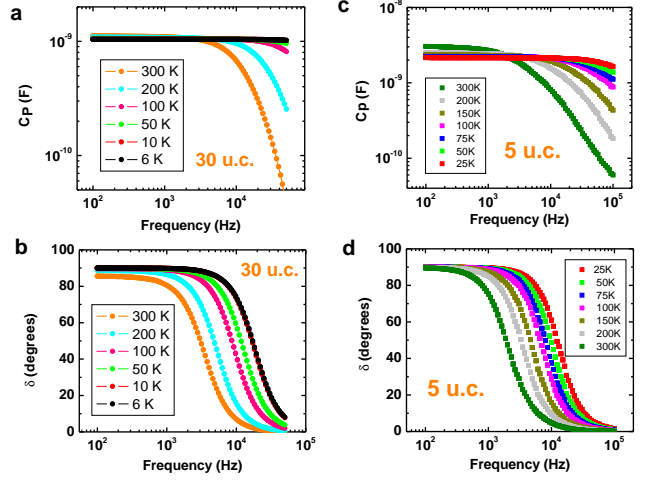


FIG. 9:  $C_P$  vs.  $f$  and  $\delta$  vs.  $f$  for both a 5 u.c. and a 30 u.c. sample showing the  $RC$  roll-off frequencies.

mentary Fig. 8b shows the complex phase angle, which remains at  $\delta = 90^\circ$ , except for a peak during the depletion transition to the low  $C$  value. Thus, the sample exhibits near ideal capacitor response throughout the applied voltage range and is qualitatively similar to the response expected for a MOS capacitor.<sup>20</sup> The dashed lines indicate the ideal and measured capacitance expected across the  $\text{LaAlO}_3$  assuming bulk dielectric constant of  $\approx 20$ . The measured capacitance gives an  $\text{LaAlO}_3$  dielectric constant of  $\approx 10$ , which is a factor of two less than expected. This is however not unusual for ultra thin films since there are voltage drops associated with the electrode-dielectric interface which strongly affect the measured capacitance.<sup>28</sup>

Supplementary Fig. 8c shows a  $CV$  curve for the same 30 u.c. sample shown in Fig. 4a of the main text. The associated  $\delta(V)$  curves are shown in Fig. 4 of the main text. For samples with thicknesses  $\geq 20$  u.c., we find that  $C_P$  and  $C_S$  diverge while  $\delta$  becomes less than  $90^\circ$ , coinciding with the onset of Zener tunneling. Thus as charge carriers are introduced into the  $\text{LaAlO}_3$  bandgap, the  $\text{LaAlO}_3$  effectively becomes a leaky dielectric. Thus we observe the sudden deviation in  $\delta$  from  $90^\circ$  while the capacitance values strongly depend on the circuit model chosen to analyze the data. In the main text, we show  $C_P$  in Fig. 4a since that is the value generally reported in the literature for MFIS or MFIM capacitors.

The measurement frequencies for all data shown in Fig. 4, main text, were 100 Hz to 10 kHz. As can be seen in Supplementary Fig. 9 these are mostly below the  $RC$  roll-off limit at 10 K.

- <sup>1</sup> Luo, W., Duan, W., Louie, S. G. & Cohen, M. L. Structural and electronic properties of  $n$ -doped and  $p$ -doped  $\text{SrTiO}_3$ . *Phys. Rev. B* **70**, 214109 (2004).
- <sup>2</sup> Shanthi, N. & Sarma, D. D. Electronic structure of electron doped  $\text{SrTiO}_3$ :  $\text{SrTiO}_{3-\delta}$  and  $\text{Sr}_{1-x}\text{La}_x\text{TiO}_3$ . *Phys. Rev. B* **57**, 2153–2158 (1998).
- <sup>3</sup> Wunderlich, W., Ohta, H. & Koumoto, K. Enhanced effective mass in doped  $\text{SrTiO}_3$  and related perovskites. *Phys. B: Cond. Matt.* **404**, 2202 – 2212 (2009).
- <sup>4</sup> Peacock, P. W. & Robertson, J. Band offsets and schottky barrier heights of high dielectric constant oxides. *J. Appl. Phys.* **92**, 4712–4721 (2002).
- <sup>5</sup> Lim, S. G. *et al.* Dielectric functions and optical bandgaps of high-K dielectrics for metal-oxide-semiconductor field-effect transistors by far ultraviolet spectroscopic ellipsometry. *J. Appl. Phys.* **91**, 4500–4505 (2002).
- <sup>6</sup> Mi, Y. Y. *et al.* Epitaxial  $\text{LaAlO}_3$  thin film on silicon: Structure and electronic properties. *Appl. Phys. Lett.* **90**, 181925 (2007).
- <sup>7</sup> Chen, W., Chulkov, E. & Paul, J. Band structure calculations of Pt and  $\text{Pt}_3\text{Ti}$ . *Phys. Scripta* **54**, 392 (1996).
- <sup>8</sup> Wolf, E. L. *Principles of Electron Tunneling Spectroscopy* (Oxford University Press, 1985).
- <sup>9</sup> Gu, X., Elfimov, I. S. & Sawatzky, G. A. The role of the band gaps in reconstruction of polar surfaces and interfaces (2009). arXiv:0911.4145v1.
- <sup>10</sup> Bykhovski, A., Gelmont, B., Shur, M. & Khan, A. Current-voltage characteristics of strained piezoelectric structures. *J. Appl. Phys.* **77**, 1616–1620 (1995).
- <sup>11</sup> Wetzel, C., Takeuchi, T., Amano, H. & Akasaki, I. Electric-field strength, polarization dipole, and multi-interface band offset in piezoelectric  $\text{Ga}_{1-x}\text{In}_x\text{N}/\text{GaN}$  quantum-well structures. *Phys. Rev. B* **61**, 2159–2163 (2000).
- <sup>12</sup> Simon, J. *et al.* Polarization-induced Zener tunnel junctions in wide-band-gap heterostructures. *Phys. Rev. Lett.* **103**, 026801 (2009).
- <sup>13</sup> Bell, C., Harashima, S., Hikita, Y. & Hwang, H. Y. Thickness dependence of the mobility at the  $\text{LaAlO}_3/\text{SrTiO}_3$  interface. *Appl. Phys. Lett.* **94**, 222111 (2009).
- <sup>14</sup> Minohara, M., Yasuhara, R., Kumigashira, H. & Oshima, M. Termination layer dependence of schottky barrier height for  $\text{La}_{0.6}\text{Sr}_{0.4}\text{MnO}_3/\text{Nb:SrTiO}_3$  heterojunctions. *Phys. Rev. B* **81**, 235322 (2010).
- <sup>15</sup> Hikita, Y., Nishikawa, M., Yajima, T. & Hwang, H. Y. Termination control of the interface dipole in  $\text{La}_{0.7}\text{Sr}_{0.3}\text{MnO}_3/\text{Nb:SrTiO}_3$  (001) schottky junctions. *Phys. Rev. B* **79**, 073101 (2009).
- <sup>16</sup> Yoshimatsu, K., Yasuhara, R., Kumigashira, H. & Oshima, M. Origin of metallic states at the heterointerface between the band insulators  $\text{LaAlO}_3$  and  $\text{SrTiO}_3$ . *Phys. Rev. Lett.* **101**, 026802 (2008).
- <sup>17</sup> Simmons, J. G. Low-voltage current-voltage relationship of tunnel junctions. *J. Appl. Phys.* **34**, 238–239 (1963).
- <sup>18</sup> Chang, I. Y.-K. & Lee, J. Y.-M. Temperature dependence of the current conduction mechanisms in  $\text{LaAlO}_3$  thin films. *Appl. Phys. Lett.* **93**, 223503 (2008).
- <sup>19</sup> Städele, M., Sacconi, F., Carlo, A. D. & Lugli, P. Enhancement of the effective tunnel mass in ultrathin silicon dioxide layers. *J. Appl. Phys.* **93**, 2681–2690 (2003).
- <sup>20</sup> Sze, S. M. *Physics of Semiconductor Devices* (Wiley-Interscience, 2006), 3 edn.
- <sup>21</sup> Fowler, R. H. & Nordheim, L. Electron emission in intense electric fields. *Proc. R. Soc. Lond. A* **119**, 173–181 (1928).
- <sup>22</sup> Zener, C. A theory of electrical breakdown of solid dielectrics. *Proc. Roy. Soc. A* **145**, 523–529 (1934).
- <sup>23</sup> Yu, P. Y. & Cardona, M. *Fundamentals of Semiconductors* (Springer, New York, 1999).
- <sup>24</sup> Jena, D., Fang, T., Zhang, Q. & Xing, H. Zener tunneling in semiconducting nanotube and graphene nanoribbon  $p-n$  junctions. *Appl. Phys. Lett.* **93**, 112106 (2008).
- <sup>25</sup> Copie, O. *et al.* Towards two-dimensional metallic behavior at  $\text{LaAlO}_3/\text{SrTiO}_3$  interfaces. *Phys. Rev. Lett.* **102**, 216804 (2009).
- <sup>26</sup> Datta, S. *Quantum Transport: Atom to Transistor* (Cambridge University Press, 2005).
- <sup>27</sup> Sancho, M. P. L., Sancho, J. M. L. & Rubio, J. *Phys. F: Met. Phys.* (1984).
- <sup>28</sup> Singh-Bhalla, G., Du, X. & Hebard, A. F. Contribution of interface capacitance to the electric-field breakdown in thin-film  $\text{Al-AlO}_x\text{-Al}$  capacitors. *Appl. Phys. Lett.* **83**, 2417 (2003).